Important Notice

UNIVERSITY OF CALGARY

SINGLE-WELL IMAGING USING FULL-WAVEFORM SONIC DATA

by

Louis Chabot

A THESIS

SUBMITTED TO THE FACULTY OF GRADUATE STUDIES

IN PARTIAL FULFILMENT OF THE REQUIREMENTS FOR THE

DEGREE OF MASTER OF SCIENCE

DEPARTMENT OF GEOLOGY AND GEOPHYSICS

CALGARY, ALBERTA

NOVEMBER, 2003

UNIVERSITY OF CALGARY

FACULTY OF GRADUATE STUDIES

The undersigned certify that they have read, and recommend to the Faculty of Graduate Studies for acceptance, a thesis entitled "Single-well imaging using full-waveform sonic data" submitted by Louis Chabot in partial fulfilment of the requirements of the degree of Master of Science.

Supervisor, Dr. R. James Brown, Department of Geology and Geophysics

Dr. John C. Bancroft, Department of Geology and Geophysics

Dr. Laurence R. Lines, Department of Geology and Geophysics

Dr. Kenneth M. Tubman, Veritas GeoServices

ABSTRACT

I am proposing a processing and imaging flow to image acoustic impedance contrasts away from the borehole wall using full-waveform data acquired with a conventional acoustic well-logging tool in an open-hole environment. The proposed flow adapts known surface-seismic processing steps and optimizes them for the borehole environment. Improvements over past flows include the use of radial filtering for linear-noise attenuation and equivalent-offset prestack time migration for imaging. 2D finite-difference and raytracing methods were used to create and test the flow on synthetic data. The flow was next applied to a full-waveform sonic dataset, recorded over a section of the 8-8-23-23W4 well, Blackfoot, Alberta, intersecting three coal seams obliquely. Although the three targeted coal seams were not very well imaged, the final composite sonic image showed promising indications of dipping interfaces elsewhere. The principal cause for this fair result was the large angle between the borehole axis and the dipping beds.

ACKNOWLEDGEMENTS

DEDICATION

In loving memories to my aunts Mesdames Eliane Dery, Gemma Dery and Denyse Dery and to my grandmother Madame Aurore Dery who all passed away during my stay in Calgary.

TABLE OF CONTENTS

LIST OF TABLES

LIST OF FIGURES

LIST OF ABBREVIATIONS AND NOMENCLATURE

BARS™ = Borehole Acoustic Reflection Survey (a Schlumberger trademark)

CMP = Common-midpoint

CSP = Common-scatter-point

DSI™ = Dipole Shear Sonic Imager (a Schlumberger trademark)

EOM = Equivalent offset migration

EVA™ = Evaluation of Velocity and Attenuation (a Schlumberger trademark)

FMI™ = Fullbore Formation MicroImager (a Schlumberger trademark)

FMS™ = Formation MicroScanner Imaging (a Schlumberger trademark)

EPIGRAPH

"There are many things in life that will catch your eye, but only a few will catch your heart….pursue those " - *Anonymous*

CHAPTER 1: INTRODUCTION

1.1   Single-well imaging

Reservoir rocks are routinely imaged using 2D or 3D surface seismic techniques. Although such techniques are effective for imaging reservoirs on a structural scale (e.g. faults), surface seismic experiences difficulties when it attempts to image the reservoir rock formation in more detail (e.g. fractures). This problem can be especially acute, for example when attempting, to place a horizontal well within a reservoir. In contrast, well-logging techniques are very effective in capturing the characteristics of the reservoir on a very small scale (e.g. bed boundaries). However, depending on the lithology and hole conditions, the well-log information can be ambiguous as, for example, in the case of dipmeter data acquired in a very rugose hole. Even when a field has good surface seismic data and well-log data, how does one bring them together? This question should not go unresolved since knowledge of the reservoir characteristics is critical for the proper exploitation of the reservoir.

Single-well imaging can contribute to reservoir understanding by helping to bridge the resolution gap between well logging and seismic data (Figure 1.1) and by extending our understanding of the reservoir characteristics to an intermediate scale.

The acoustic well-logging tool provides a unique acquisition geometry whereby both source and receivers are in the same borehole, several receivers are located at different offsets along the body of the well-logging tool (Figure 1.2) and, as the well-logging tool is moved uphole, the rock formations surrounding the borehole are sampled

repeatedly. This acquisition geometry can be analogous to a *single-well imaging* experiment.

This technique is not to be confused with the more traditional single-well-seismic imaging survey, which is acquired by using a downhole seismic source (e.g. a downhole hydraulic vibrator) with a series of clamped receivers in the same borehole to image, for example, the flank of a salt dome (Chen, 1993; Peveraro *et al.*, 1994). The focus of this work is on single-well imaging using a conventional acoustic well-logging tool.

The single-well imaging technique using a well-logging tool has the advantage of requiring only one borehole (in contrast to crosswell seismic), one instrument (in contrast to vertical seismic profiling) and the full-waveform data are available wherever a sonic log has been acquired (the full waveform is obtained simultaneously with the acquisition of the compressional and shear velocity logs).
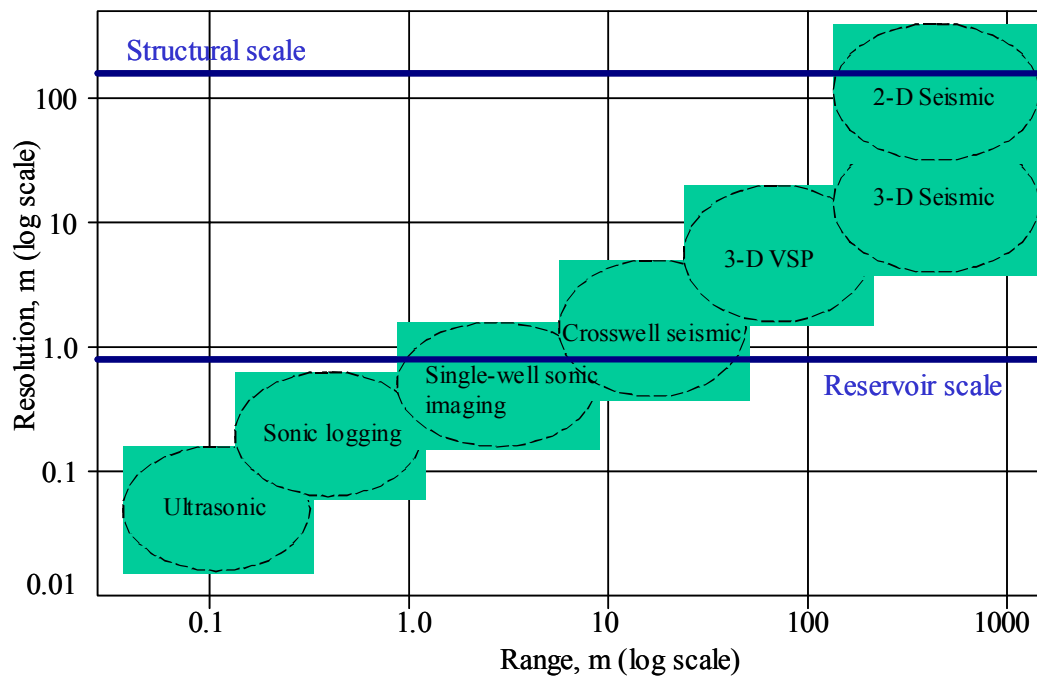
FIGURE 1.1. Single-well sonic imaging bridging the resolution gap between well-logging and seismic data (modified after Chang et al., 1998).

1.2   Acoustic well logging and full waveforms

With the help of a string of hydrophones located at different distances or offsets from the transmitter, the acoustic well-logging tool records the complete pressure wave propagating in a fluid-filled borehole generated by an impulsive source transmitted in the same borehole (Figure 1.2). The borehole fluid or drilling mud provides the acoustic coupling between the rock formation, making up the borehole wall, and the well-logging tool. The complete acoustic pressure signal is sensed and recorded by the hydrophone or receiver at a fixed sample rate for a certain length of time and the resulting recorded signal is called the *full waveform*. There is a full waveform recorded at each receiver. Each full waveform contains several pressure signals such as direct or fluid waves, P and S head waves, pseudo-Rayleigh waves, Stoneley waves, normal modes as well as converted modes. Head waves are refracted body waves at the critical angle. Presently both the P-wave and S-wave velocities are routinely extracted by different methods (e.g. Willis and Toksöz, 1983) from those full waveforms used to generate P-wave and S-wave well-log curves versus depth.

The knowledge of the P- and S-wave velocities plays an important role in identifying the lithology of a rock formation (e.g. V_P/V_S ratio), in determining the mechanical properties of a rock formation (e.g. Poisson's ratio), and in creating synthetic seismograms (when density information is available) for seismic interpretation. Full waveforms can be acquired either in cased hole to quantify the quality of the cement bond (Tubman *et al.*, 1986) or in uncased hole, or *open hole*. This work focuses on the full waveform acquired in an open hole.
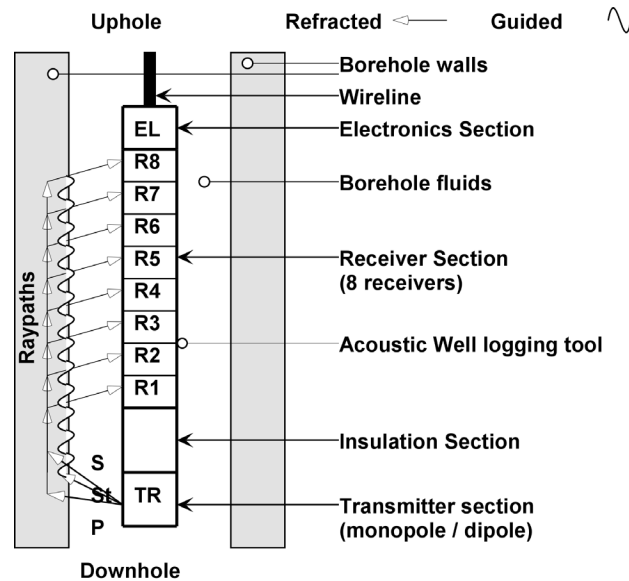
FIGURE 1.2. Typical acoustic well-logging tool configuration in a fluid-filled borehole.

1.3   Previous work on single-well sonic imaging

There have been previous attempts at single-well imaging using acoustic well-logging tools (Hornby, 1989; Fortin *et al.*, 1991; Watanabe *et al.*, 1998).

Hornby (1989) used an experimental acoustic well-logging tool equipped with one monopole source and twelve hydrophone receivers to compute an image of structural changes beyond the borehole wall. Details of the tool geometry are provided in Table 1.1. With the source and receiver array both passing through the structures that cross the borehole, downdip and updip structures could be imaged separately.

In his single-well imaging effort, Hornby (1989) removed the P and S head waves, and the Stoneley waves arrivals from individual shot records using an *f-k* filter. Then, he applied a migration algorithm to the prestack filtered sonic data. This migration algorithm, called a "backprojection operator", bins the waveform data into either the updip or the downdip side of the borehole based on the raypath. The processing imaging

effort is detailed in Table 1.2. Although this method introduces the concept of migrating the waveform, there is no mention of the application of statics and/or deconvolution to the data. In addition, the data may have suffered from both time and spatial aliasing due to the coarse time (20 μs) and spatial sampling (0.15 m).

TABLE 1.1. Single-well sonic imaging: tool geometries.

Well-logging tool designation	Prototype acoustic logging tool (Hornby, 1989)	EVA™ (Fortin *et al.*, 1991)	BARS™ (Watanabe *et al.*, 1998)
Number of transmitters	1 monopole	4 monopoles	1 or 3 monopoles
Frequency band	5-18 kHz	3–25 kHz	8-30 kHz (?)
Number of receivers	12	12	8
Near to far offsets	3.35 to 5 m	1 to 12.75 m	4.4 to 16 m
Receiver spacing	0.15 m	1.00 m	0.15 m
A/D converter	12 bits (?)	11 bits plus sign	16 bits (?)
Data sampling rate	20 μs	5 or 10 μs	10 μs (?)
Waveform recorded	20 ms	Up to 12.5 ms	12 ms
Shot spacing, or logging speed and shot firing rate.	0.15 m 9.14 m/min 1000 ms	(unknown), 4.8 m/min 65 ms (?)	(unknown), 6 m/min (unknown)

Although the Evaluation of Velocity and Attenuation or EVA™ array sonic logging tool was introduced by Arditty *et al.* (1981), credit for the single-well imaging effort goes to Fortin *et al.* (1991) who used the EVA™ logging tool to attempt to image acoustic contrasts away from the wellbore. Details of the EVA™ tool geometry are

provided in Table 1.1. The proposed imaging-processing flow hinges on the separation, in the shot records, of the reflected waves originating from beneath the well axis to the reflected waves originating from above the well axis using velocity-filtering techniques. Once separated, two distinct families of gathers were created. Both families of gathers were afterwards processed separately in the following fashion: additional filtering, normal-moveout correction and common midpoint stacking. Finally the two processed sections were reunited along their zero line to form a sonic image. The processing imaging effort is detailed in Table 1.2. However, this method did not include the use of statics, deconvolution or migration in the processing-imaging flow.

Watanabe *et al.* (1998) used a Borehole Acoustic Reflection Survey or BARS™ sonic logging tool to image reflectors beyond the borehole wall in horizontal or deviated wells. The BARS™ is a research sonic logging tool, which is a modified version of the existing commercial dipole shear-sonic imager or DSI™ tool (Esmeroy *et al.*, 1998). The BARS™ tool geometry is provided in Table 1.1, while the details of the full-waveform processing are provided in Table 1.2. Note that both the poststack and prestack migration techniques used are based on the generalized Radon transform and are similar to conventional Kirchhoff migration (Miller *et al.*, 1987). Although the processing flow generated images of good quality, especially in horizontal borehole (Coates *et al.*, 2000), the details of the processing flow used to achieve these results were sketchy at best.

TABLE 1.2. Single-well sonic imaging: full-waveform processing steps.

Well-logging tool designation	Prototype acoustic logging tool (Hornby, 1989)	EVA™ (Fortin *et al.*, 1991)	BARS™ (Watanabe *et al.*, 1998)
Static corrections	No	No	No (?)
Filtering	Removal of signal below 2 kHz. Removal of, refracted P and S, and Stoneley arrivals by *f-k* filtering.	Low cut filter to attenuate Stoneley and S-Rayleigh. Wavefield separation by velocity filtering (reflections from beneath and above)	Removal of refracted P and S, and Stoneley arrivals by bandpass and *f-k* dip filtering.
Deconvolution	No	No	Yes (?)
Normal moveout	Yes (?)	Yes	Yes
Common midpoint stack	Yes (6 fold) (?)	Yes (16 fold)	Yes (8 fold)
Migration	Prestack back-projection operator	No	Poststack or prestack based on generalized Radon transform
Angle between the borehole axis and the intersecting beds	43°	15° to 35°	0° (near-horizontal well) to 30°
Imaging distance from borehole axis	18 m	7 m	10 m

1.4   Goal

This work investigates the acoustic and elastic-wave propagation in and around an open borehole, using the full waveform acquired with a conventional sonic logging tool using a monopole source, with the purpose of creating a processing-imaging flow applicable to full-waveform sonic data to image reflected energy originating from acoustic impedance contrasts from beyond the borehole walls. The acoustic impedance contrasts could take the form of either lithological changes or fractures (Haugen and Schoenberg, 2000). Resolving these features could improve our knowledge of a reservoir that is not easily seen in the surface seismic data. Single-well imaging offers the possibility to image key structural information in different wells and structural-domain changes not evident from surface seismic data. In addition, single-well sonic imaging could also be applicable in determining the proximity of the top of the reservoir in horizontal drilling.

1.5   Structure of the thesis

The thesis is structured as seven distinct chapters. Chapter 1 introduces and defines key terms and give the motivation of this research. Chapter 2 provides the background on the different modes present in the full waveform acquired by the well-logging tool. It then goes on to introduce the finite-difference model to explore the variation of those different modes with offset. In addition Chapter 2 provides the interpretive insights into the complex and visually overwhelming full-waveform data acquired by an acoustic well-logging tool. Chapter 3 introduces the notion of simplifying the 3D borehole-geometry problem into a 2D borehole-geometry problem for simple shapes. Next the results of the proposed processing flow for 2D on synthetic data are

shown. Chapter 4 shows how the full-waveform field data were acquired and its interpretation with conventional methods. Chapter 5 provides a step-by-step description of the proposed full-waveform processing flow on field data. Chapter 6 compares the composite sonic image with the surface seismic data. Finally, Chapter 7 gives conclusions and recommendations for future work coming out of this exciting project.

CHAPTER 2: ELASTIC WAVE PROPAGATION IN A FLUID-FILLED BOREHOLE

2.1   Individual wave modes in the full waveform

The rigorous mathematical treatment of acoustic-wave propagation in a fluid-filled borehole has been covered in detail by Cheng and Toksöz (1981), Paillet and Cheng (1991) and others and is not discussed here. Instead, the individual wave modes in the full waveform and the known factors influencing their amplitudes, phases and velocities are introduced and discussed in this section. The knowledge derived from this will be important not only in recognizing the different wave modes present (or absent) in the full-waveform field records, but also will be critical in selecting the appropriate processing-imaging strategy, which will be discussed in subsequent chapters.

First, let's explore conceptually the propagation of acoustic waves in the borehole fluid and the propagation of elastic waves in the formation around the borehole. In the typical case of a fluid-filled borehole, the rock formation has compressional velocity, V_P, greater than the shear velocity, V_S, which in turn has a velocity greater than the compressional fluid velocity, V_f. When an azimuthally symmetric pressure source, or *monopole* source, radiates a compressional pulse out into the borehole fluid, the following can be observed (Figure 2.1). Initially this pulse generates a wave in the borehole fluid. This fluid wave propagates at a speed of V_f, and eventually reaches the borehole wall, where it excites both compressional and shear waves in the formation. At this point some energy is reflected back into the borehole and some is critically refracted and transmitted. The critically refracted compressional and shear waves constitute head

waves, which propagate back into the borehole at speeds of V_P and of V_S, respectively.

On the other hand, as the transmitted compressional and shear waves propagate in the formation, they are likely to encounter acoustic-impedance contrasts, which are likely to scatter energy back towards the borehole where the receivers of the well-logging tool are located. In addition, because of the geometric properties of the fluid-filled borehole, allowing for both partial and complete trapping of wave energy, additional wave modes are created in the borehole, namely the pseudo-Rayleigh and Stoneley waves, which are also recorded in the full waveform.
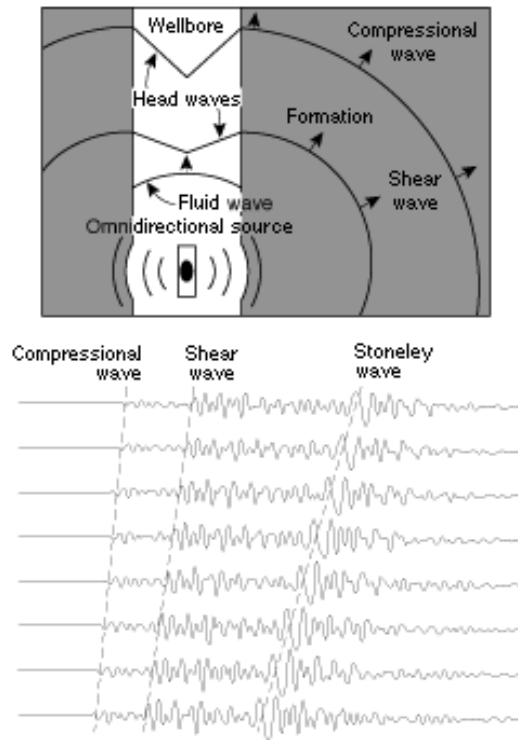
FIGURE 2.1. Cross-section through the borehole illustrating the acoustic- and elastic-wave propagation in the borehole fluid and in the formation around the borehole (for $V_P > V_S > V_f$). The corresponding theoretical recorded wavetrain at the well-logging tool for different offsets along the borehole axis is also shown (after Schlumberger, 1997).

Each wave mode displays a specific behaviour and these are summarized in Table 2.1. Note that each wave mode in the full waveform is recorded at a distance of several wavelengths away from the source, which may be considered as the far field.

The critically refracted P and S arrivals, or *head waves*, have been used significantly in borehole acoustic logging to calculate V_P and V_S. The tube wave is a coupled wave mode intrinsically involving both the fluid and the wall of the borehole, which expands and contracts as the pressure wave passes. Most tube waves travel axially, their amplitudes decreasing slowly with distance as they travel along the borehole axis.

Stoneley waves propagate along the borehole wall and die away exponentially into the formation surrounding the borehole. In particular, Stoneley waves are, in general, slightly dispersive with both group and phase velocities close to 0.8 to 0.9 times V_f. Stoneley waves are present at all frequencies. At higher frequencies (> 30 kHz) the Stoneley-wave velocity approaches V_f. Interestingly; borehole Stoneley waves can be used for estimation of the formation permeability along the well (Brie *et al.*, 2000).

On the other hand, the pseudo-Rayleigh waves cannot exist below a minimum frequency where their velocity equals V_S (Sheriff and Geldart, 1995). Pseudo-Rayleigh waves propagate along the borehole wall and die away exponentially into the formation surrounding the borehole. As the borehole radius increases, the pseudo-Rayleigh dispersion curve is shifted towards lower frequency. At higher frequencies (> 30 kHz) the velocity of the pseudo-Rayleigh waves approaches V_f. The pseudo-Rayleigh wave differs from the classical Rayleigh surface wave in that an external fluid medium is available for radiating energy away from the solid (Tsang and Rader, 1979). The pseudo-Rayleigh and

the shear head waves have such similar velocities that often they arrive too close to one another to be distinguished.

TABLE 2.1. Summary of principal wave modes in the borehole (for $V_P > V_S > V_f$).

Wave name	P-head wave	S-head wave	Pseudo-Rayleigh	Direct or Fluid	Stoneley
Type	Body wave	Body wave	Guided by the borehole	Body wave	Guided by the borehole
Strength	Low amplitude	Moderate amplitude	High amplitude	Low amplitude	High amplitude
Amplitude	Geometric spreading and Q	Geometric spreading and Q and a shear velocity greater than fluid compression-al velocity	Decays exponentially with distance away from borehole wall and oscillatory in the fluid		Decays exponentially with distance away from borehole wall Decreases slowly with axial distance
Velocity (phase and group)	Velocity independent of frequency	Velocity independent of frequency	Velocity dependent on frequency	Velocity independent of frequency	Velocity slightly dependent on frequency
Velocity	V_P	V_S	Approaches S velocity at low f	V_f	Approx. 0.8 to 0.9 of V_f

The compressional and shear head waves exhibit a linear variation of acoustic energy with offset or *linear moveout* when the receivers are located along the borehole axis; similarly for the pseudo-Rayleigh and Stoneley waves. On the other hand, scattered energy coming from acoustic-impedance contrasts away from the borehole wall does not exhibit linear moveout. In addition, the amplitude of scattered energy is generally smaller than that of refracted energy.

Individual wave modes in the full waveform, recorded by the receivers located along the borehole axis, are also dependent on: the source wavelet, the characteristics of the logging tool, the borehole diameter (e.g. number and character of trapped modes), the fluid properties, and the formation properties. The impact of these different factors on the full waveform can best be observed through the use of synthetic borehole microseismograms (Paillet and Cheng, 1991).

Figure 2.2 shows an example of the effect of lithologies on the full waveform by comparing eight microseismograms generated for different lithologies. Keeping other factors constant, as the Poisson's ratio is reduced from 2.0 (case a) to 0.4 (case b), effectively going from a hard crystalline basalt to a soft homogeneous shale, the full-waveform changes in both amplitude and character. The shear mode disappears for $V_S <$ V_f (for cases f, g and h). The waveforms in Figure 2.2 do not include the effects of attenuation.

Additional examples of the effects of the source wavelet, the characteristics of the logging tool, and the borehole diameter on the recorded full waveform have been provided by Biot (1952), Tsang and Rader (1979), Paillet and White (1982), Paillet and Cheng (1991), and others.
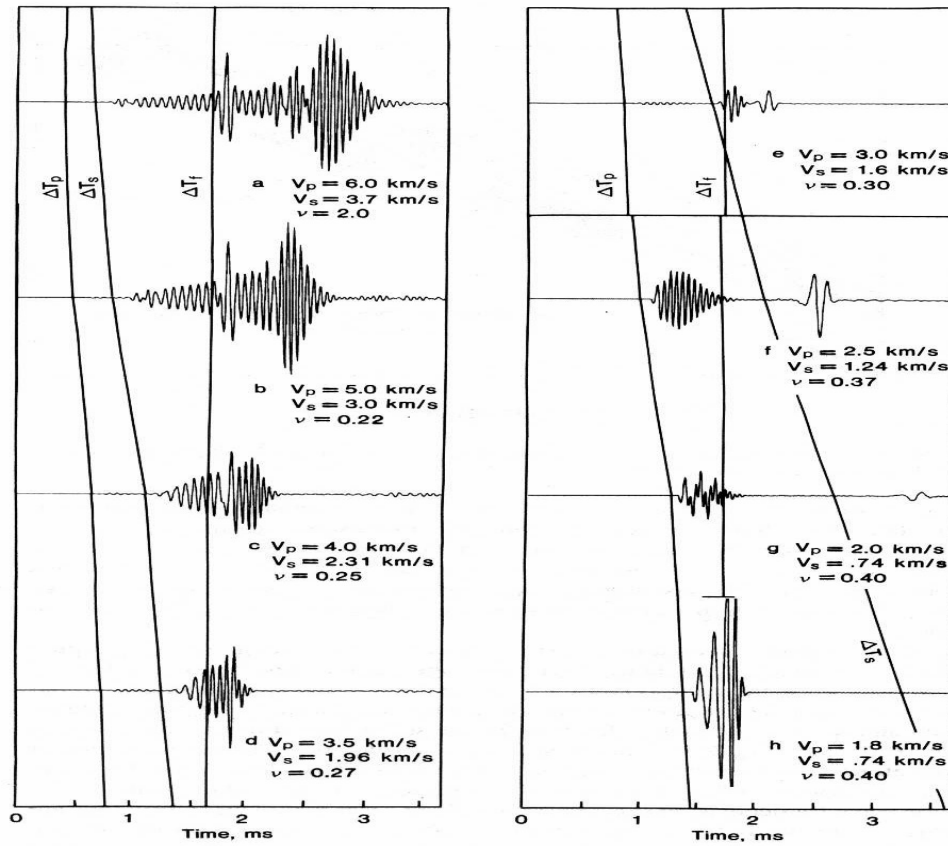
FIGURE 2.2. Synthetic borehole microseismograms for eight different lithologies with other factors kept constants (Paillet and Chen, 1991).

2.2   The finite-difference method

To yield insight into the propagation of waves from a monopole source in a fluid-filled borehole and the behaviour of the full waveform with offset, it was important to carry out numerical modelling of acoustic-wave propagation in a fluid-filled borehole. There exist in the literature 3D elastic finite-difference methods to simulate wave propagation in a borehole environment (Yoon and McMechan, 1992: Cheng *et al.*, 1995; Liu *et al.*, 1996) but no corresponding coded programs were available to me at the time of this research.

As an alternative, for this particular application, a 2D finite-difference modelling code was selected where the formulation is fourth-order in space and second-order in time. The finite-difference code selected was written by G.T. Schuster, J. Xu and Y. Luo (University of Utah) and is based on an algorithm described by Levander (1988). Additional modifications to the code were made by Guevara (2001). The advantages of the staggered-grid scheme of this algorithm lie in its stability and accuracy for modelling materials with large Poisson's ratios and mixed acoustic-elastic media (Levander, 1988).

It is important to recognize that, although a two-dimensional model does not totally capture the cylindrical geometry of the borehole environment, the fluid-layer analogy of the two-dimensional model gives a very good qualitative approximation to the physical mechanism of mode trapping and constructive interference that characterizes waveform logs (Paillet and Cheng, 1991); in other words, it provides for propagating modes that are similar to those for the fluid-filled borehole (Paillet and White, 1982).

In building the finite-difference model in a 2D Cartesian system, care was taken to choose the grid size, Δz, and the time step, Δt, so as to respect the minimum wavelength, λ_{min}, and the stability criterion, S, as described in equations (2.1) and (2.2) in order to avoid grid dispersion problems and numerical instability. The value of the stability criterion in equation (2.2) is about 1 percent lower than the theoretical stability criterion of $\sqrt{3/8}$ for second-order system in time and fourth-order in space finite differences (Lines et al., 1999). In these equations, Δz denotes the selected space step in both the vertical and horizontal directions (note that $\Delta z = \Delta x$); Δt denotes the selected time step, f_d is the dominant frequency of the energy source, while V_{min} and V_{max} represent the minimum and the maximum velocities of the model.

$$\lambda_{min} \ \Rightarrow \ \frac{V_{min}}{2.5 \ f_d} > 5 \ \Delta x \qquad (2.1)$$

$$S \Rightarrow \frac{V_{max}}{\Delta z}\Delta t \ < 0.606 \, . \qquad (2.2)$$

The finite-difference program outputs peak particle velocity in the z- and x-directions only. Although an output in pressure would have been desirable, the model outputs of velocity can be considered equivalent to pressure, since particle velocity and pressure are in phase or exactly out of phase with each other depending on the direction of travel (Brown *et al.*, 2002). The amplitudes of velocity and pressure will, however, be different. Thus the simulation results are shown for both z and x directions. Also, all the simulation results shown in the common-shot gather domain in Chapters 2 and 3 are displayed with zero time corresponding to the initiation time of the Ricker wavelet.

2.3 Variation of acoustic energy with offset in a homogeneous isotropic borehole model

The base model is two-dimensional, characterized by a vertical fluid layer confined on either side by identical elastic layers. The vertical fluid layer simulates the fluid-filled borehole. The source and receiver arrays of the well-logging tool are centred along the borehole axis in the fluid. The effects of the well-logging tool are not accounted for in this model.

The numerical model here is scaled up relative to the field, unlike most physical modelling in which the models are instead scaled down (Ebrom and McDonald, 1994). The upscaling was required because the finite-difference method results were imported into ProMAX™ for further processing, while those same results were compared with

NORSAR™ raytracing results. The ratio of lengths of geological features to the wavelength should be the same in both the model and the field (Ebrom and McDonald, 1994). A scale factor of 333 to 1 for lengths (modelled length to field length) was used to replicate the borehole environment in its main features. The dominant frequency for the modelling used was 30 Hz in comparison to the dominant frequency of the monopole source of a well-logging tool at 10 kHz. The base model dimensions are 3000 m in length (corresponding to field length of 9 m) by 1000 m in width (corresponding to field width of 3 m). The borehole model has a radius, r, of 100 m (corresponding to field radius of 0.3 m). As shown in Figure 2.3, the borehole layer is filled with a fluid that has a compressional velocity, V_f, of 1000 m/s and a density, ρ_f, of 1000 kg/m^3. The medium located immediately on either side of the borehole fluid has a compressional velocity, V_{P1}, of 2500 m/s, a shear-velocity, V_{S1}, of 1500 m/s, and a density, ρ_1, of 2000 kg/m^3.

Two source models, the first one a line source and the second one a plane-wave source, were available to simulate the pressure force of the monopole source transmitter. The source model that was the most suited for our application was the z-component line-source particle-velocity model, which is polarized in the z-direction (i.e. in the direction of the borehole axis). The wavelet selected with this line source was a zero-phase Ricker wavelet with a 30-Hz dominant frequency having duration of 67 ms. Although the Ricker wavelet is not closely related to the known response of piezoelectric sources (Tsang and Rader, 1979), it has been used extensively in the seismic literature to represent impulse sources and its mathematical properties are well known. The line source was located in the fluid-filled borehole at a point on the borehole axis.
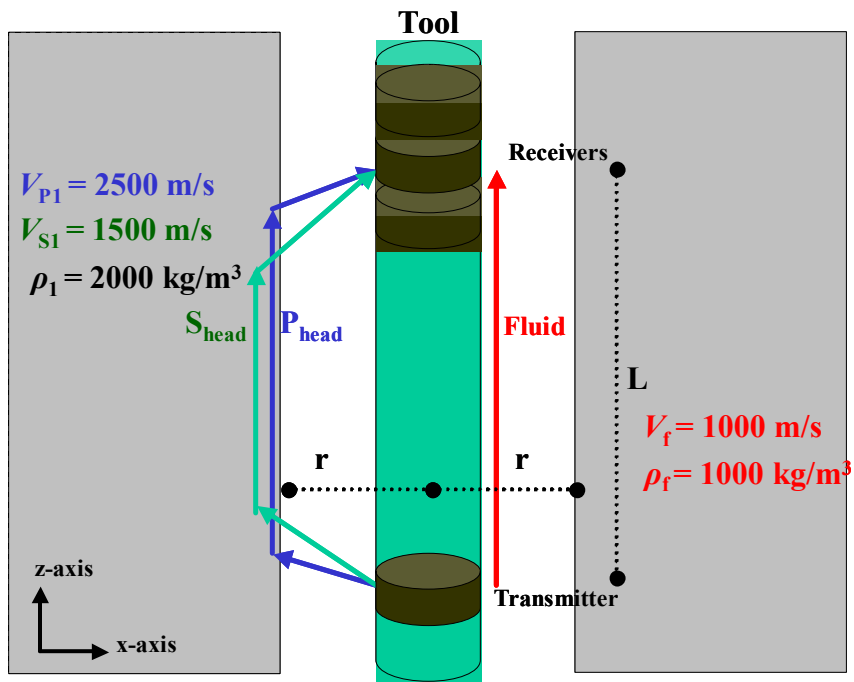
FIGURE 2.3. Diagram showing the borehole model with homogeneous isotropic media for fluid and rock.

A series of receivers were placed along the borehole axis to record the *z*- and *x*-components of particle velocity. A receiver spacing of 10 m (field 0.03 m) was used. The listening time at each receiver was 1600 ms (4.8 ms). Because the well-logging tool is not accounted for in the borehole, the receivers lie suspended in the fluid-filled borehole.

The wavefield generated by the finite-difference modelling calculation was captured at fixed time intervals to produce instantaneous views of the wavefield or snapshots. This series of snapshots was next studied for all the events. Figure 2.4 shows a sample snapshot of the wavefield at 800 ms (field 2.4 ms). Note that it took normally several hours to generate each shot record on an Ultra 60 Sun system.

The snapshot in Figure 2.4 displays the wavefield in the borehole fluid and in the surrounding elastic media at a time of 800 ms (field 2.4 ms) in two formats. The left

portion shows the vertical component (particle motion in the *z*-direction, positive upward) of the wavefield while the right portion shows the horizontal component (particle motion in the *x*-direction, positive rightward) of the same wavefield. In this snapshot, the vertical or *z*-axis represents distance along the borehole axis in metres, while the horizontal or *x*-axis represents the radial distance perpendicular to the borehole axis in metres. Undisturbed borehole fluid and formation are represented in uniform grey colour. Components of particle velocity in the borehole fluid and formation are represented as normal polarity on a grey scale from white (negative) to black (positive). Note that an amplitude cut-off was selected low enough to show waveforms of all amplitudes.
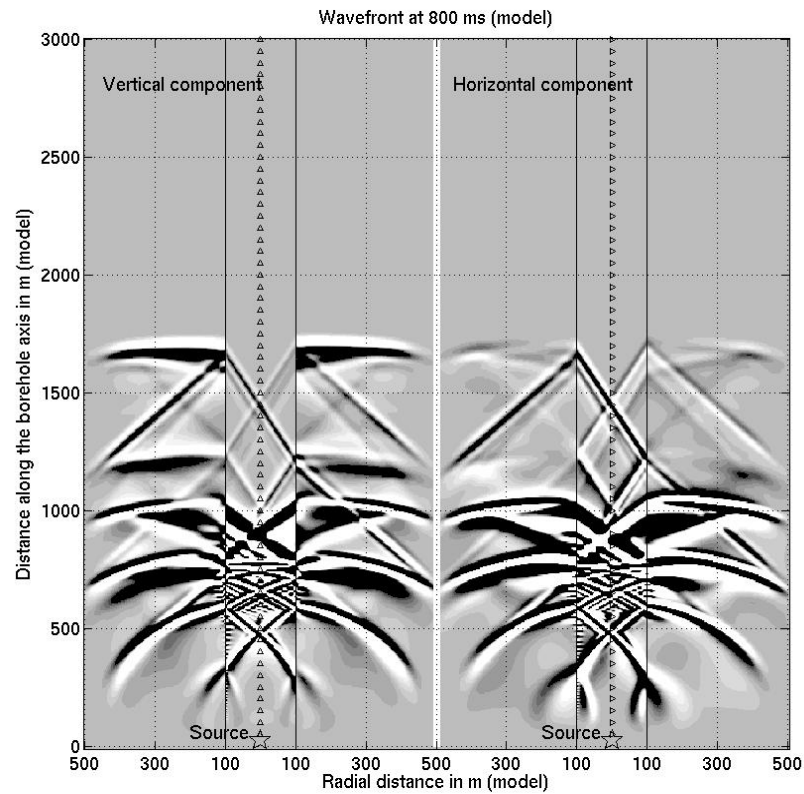
FIGURE 2.4. Snapshot of the wavefield at 800 ms (field 2.4 ms) generated by the finite-difference method. Shown are model times and distances.

The resulting change of the full waveform with offset is shown in Figure 2.5. Similarly, an amplitude cut-off was selected low enough to show waveforms of all amplitudes. Note that the number of traces in the simulation results is much larger than what is normally recorded by a conventional logging tool. Such a tool normally records a few traces within the offset range of the dashed rectangular area in Figure 2.5.
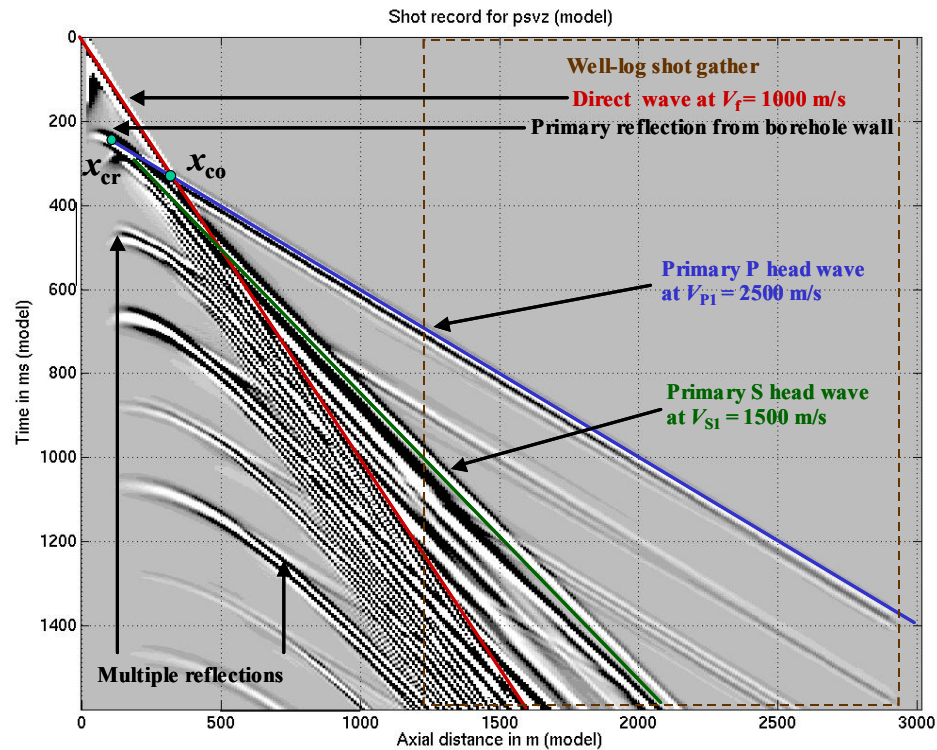
FIGURE 2.5. Common-shot gather recorded by the receivers on the borehole axis of the wave propagation in a fluid-filled borehole for a homogeneous isotropic medium. Important events are labelled. Shown are model times and distances.

For a receiver located on the axis of a borehole of uniform radius, r, at source-receiver offset, L, equations (2.3) to (2.8) provide key relations to calculate the different traveltimes associated with the arrivals of the P-wave, and similarly for the S-wave. It is important to note that the presence of the well-logging tool is not considered in the modelling. Equation (2.3) calculates the traveltime of the direct arrival in the fluid, or t_d.

Equation (2.4) calculates the traveltime of the reflected arrival from the borehole wall,

or t_r. The traveltime of the compressional head wave, or t_P, is described by equation (2.5)

while that of the shear head wave, t_S, is described by equation (2.6). The critical angle of

incidence for the compressional head wave is denoted as θ_{cP} and for the shear head wave

as θ_{cS}. Finally, the distance from the source at which the head wave is initiated, or the

critical distance, x_{cr} is shown in equation (2.7), while the crossover distance, or the point

at which the refracted wave overtakes the direct wave, is x_{co} as shown in equation (2.8).

These are given by:

$$t_d = \frac{L}{V_f} \tag{2.3}$$

$$t_r^2 = t_0^2 + \frac{x^2}{V_f^2} \quad \text{where} \quad t_0 = \frac{2\,r}{V_f} \tag{2.4}$$

$$t_P = \frac{L}{V_{P1}} + \frac{2\,r\cos\theta_{cP}}{V_f} \quad \text{where} \quad \theta_{cP} = \sin^{-1}\left(\frac{V_f}{V_{P1}}\right) \tag{2.5}$$

$$t_S = \frac{L}{V_{S1}} + \frac{2\,r\cos\theta_{cS}}{V_f} \quad \text{where} \quad \theta_{cS} = \sin^{-1}\left(\frac{V_f}{V_{S1}}\right) \tag{2.6}$$

$$x_{cr} = 2\,r\left(\left(\frac{V_{P1}}{V_f}\right)^2 - 1\right)^{-1/2} \tag{2.7}$$

$$x_{co} = 2\,r\left(\frac{V_{P1}+V_f}{V_{P1}-V_f}\right)^{1/2} \tag{2.8}$$

The compressional and shear velocities calculated from the variations of

traveltime with offset observed in Figure 2.5 are in agreement with the model parameters;

similarly for the critical and the crossover distances. Note that for the condition of $V_P >$

$V_S > V_f$ the compressional wave always travels over a longer rock path than the corresponding shear wave for a given fixed source-receiver offset. Also, as the critical angle increases, the head wave travels a decreasing distance through the rock. In addition, no shear waves will be mode-converted and critically refracted if the rock shear velocity is less than the fluid velocity.

In the event that either the well-logging tool is not well centralized in the circular borehole or the well-logging tool is centralized in a borehole with a non-circular cross section (e.g. elliptical borehole), the effects of this departure from the ideal geometry on the recording of the full waveform are as shown in Figure 2.6.
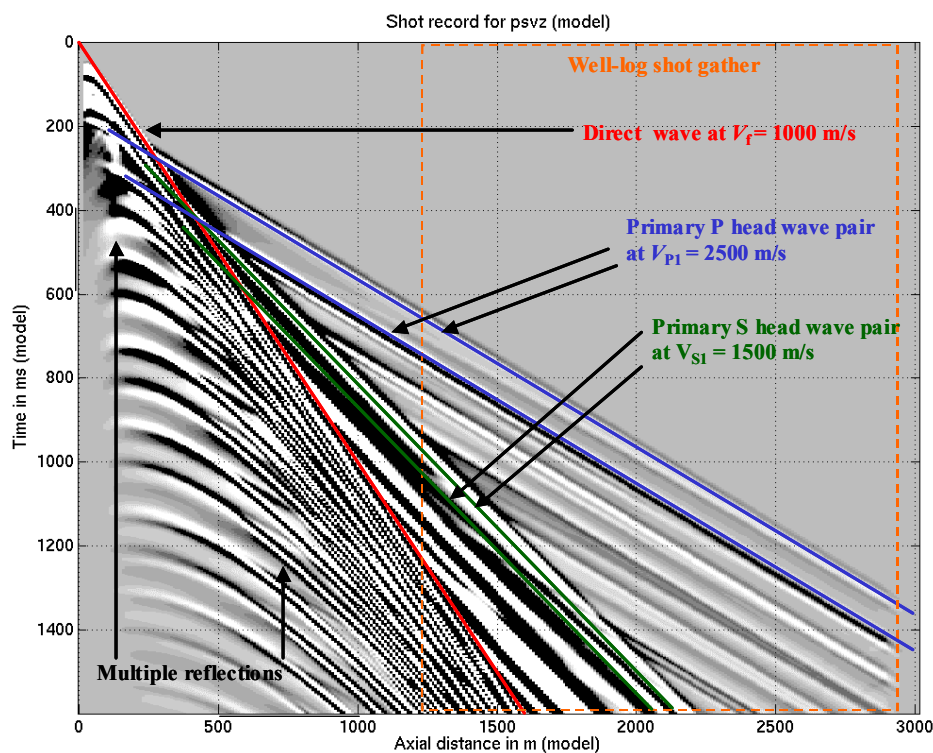
FIGURE 2.6. Common-shot gather, recorded by receivers off-centre from the borehole axis, of the wave propagation in a fluid-filled borehole for a homogeneous isotropic medium. Important events are labelled. Shown are model times and distances.

The effect of this non-ideal geometry is that either the same wavefield is sampled twice by the same receivers, in the case of the non-centralized well-logging tool, or the wavefield in the short axis arrives at the receiver slightly earlier than the wavefield in the long axis. The net results create either a pair of arrivals or smeared arrivals. The observed waveform can be further distorted by the interferences between multiple modes of refracted head waves excited by a broadband source (Paillet and Chen, 1991).

2.4 Variation of acoustic energy with offset in a borehole model with an interface perpendicular to the borehole axis

In this section, the borehole model dimensions are the same as in the previous section with the exception that an interface perpendicular to the borehole axis is added to the model (Figure 2.7).
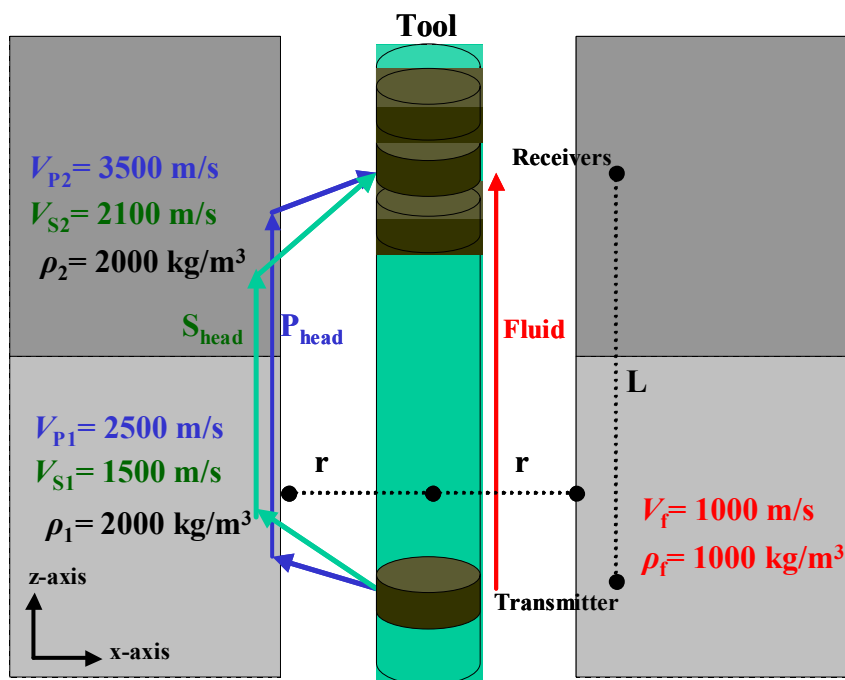
FIGURE 2.7. Diagram showing the borehole model with an interface perpendicular to the borehole axis.

In this model, the medium located above the interface on either side of the borehole fluid has a compressional velocity, V_{P2}, of 3500 m/s, a shear-velocity, V_{S2}, of 2100 m/s and a density, ρ_2, of 2000 kg/m^3. The medium located below the interface has a compressional velocity, V_{P1}, of 2500 m/s, a shear-velocity, V_{S1}, of 1500 m/s and a density, ρ_1, of 2000 kg/m^3. The borehole layer is filled with a fluid that has a compressional velocity, V_f, of 1000 m/s and a density, ρ_f, of 1000 kg/m^3. The model dimensions and the survey parameters are unchanged from the previous section.
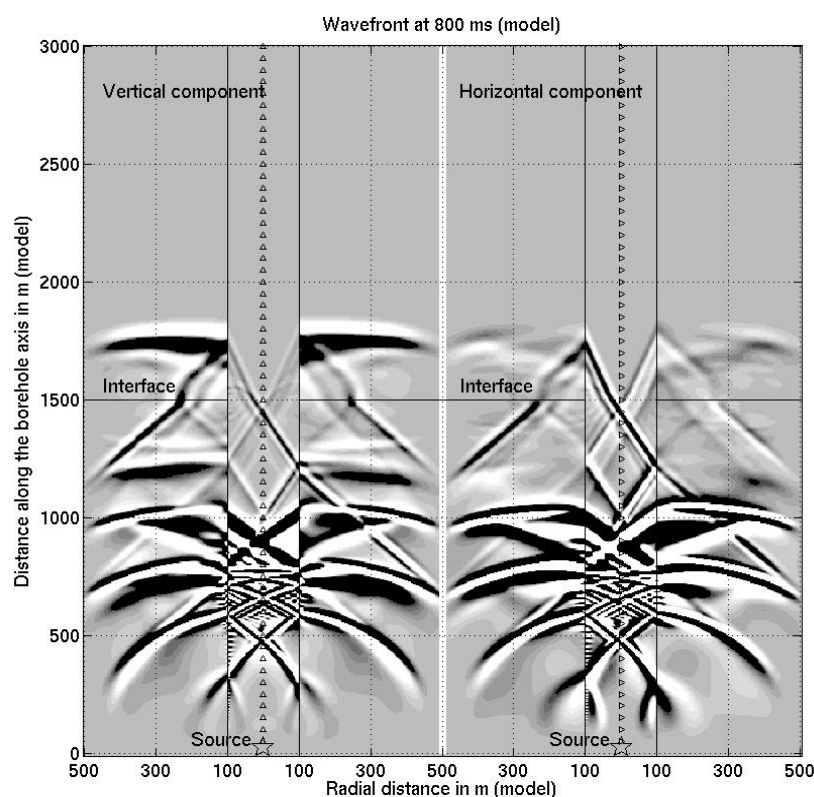
FIGURE 2.8. Snapshot of the wavefield at 800 ms (field 2.4 ms) generated by the finite-difference method. Shown are model times and distances.

The wavefield generated by the finite-difference modelling calculation was also captured at fixed time intervals. This generated a series of snapshots that were next

studied. Figure 2.8 shows a sample snapshot of the wavefield at 800 ms (field 2.4 ms).

An amplitude cut-off was selected low enough to show waveforms of all amplitudes.

The resulting change of the full waveform with offset is shown in Figure 2.9. The compressional and shear velocities, on either side of the interface, calculated from the various arrival times with varying offset observed in Figure 2.9, are in agreement with the model parameters. When the source-receiver pair straddles the interface, the compressional and shear arrivals can be computed using the following:

$$t_P = \frac{L_1}{V_{P1}} + \frac{r\cos\theta_{cP1}}{V_f} + \frac{L_2}{V_{P2}} + \frac{r\cos\theta_{cP2}}{V_f}$$

$$\text{where } \theta_{cP1} = \sin^{-1}\left(\frac{V_f}{V_{P1}}\right) \text{ and } \theta_{cP2} = \sin^{-1}\left(\frac{V_f}{V_{P2}}\right)$$

(2.9)

$$t_S = \frac{L_1}{V_{S1}} + \frac{r\cos\theta_{cS1}}{V_f} + \frac{L_2}{V_{S2}} + \frac{r\cos\theta_{cS2}}{V_f}$$

$$\text{where } \theta_{cS1} = \sin^{-1}\left(\frac{V_f}{V_{S1}}\right) \text{ and } \theta_{cS2} = \sin^{-1}\left(\frac{V_f}{V_{S2}}\right)$$

(2.10)

$$\text{where } L = L_1 + L_2$$

(2.11)

When the transmitter-receiver pairs span an interface separating two distinct lithologies, the effects of this can be observed (Basick, 1983) as seen in Figure 2.9.
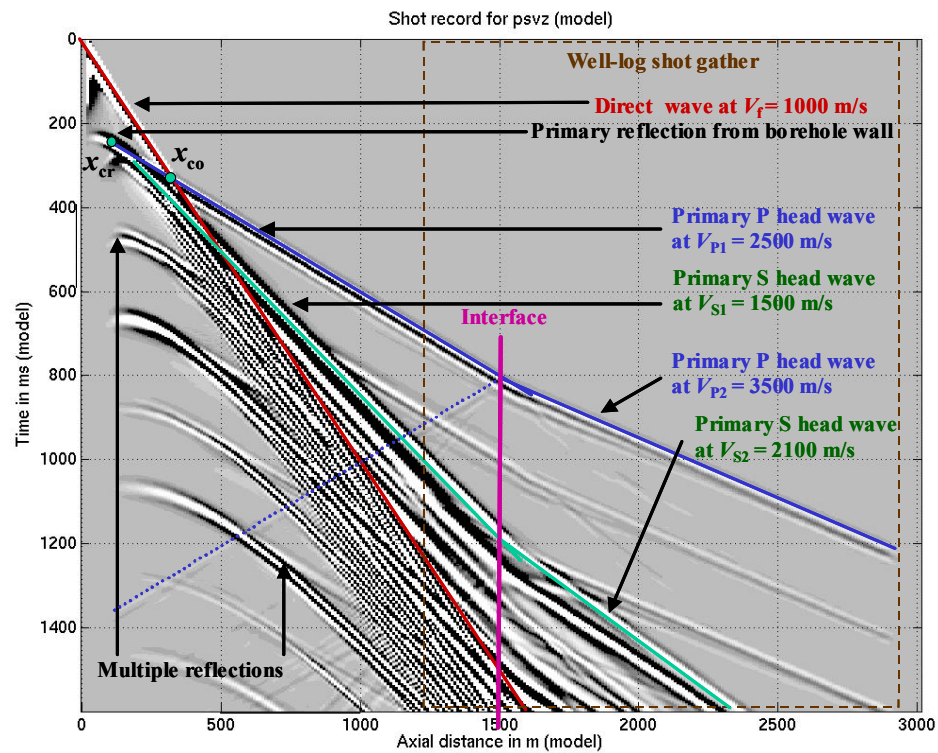
FIGURE 2.9. Common-shot gather recorded by the receivers on the borehole axis of the wave propagation in a fluid-filled borehole with an interface perpendicular to the borehole axis. Important events are labelled.

CHAPTER 3: PROCESSING AND IMAGING OF SINGLE-WELL SONIC FULL WAVEFORM SYNTHETIC DATASET

3.1 Simplification of the 3D borehole geometry into a 2D borehole geometry for simple shapes

Knowing that I had access to a valid 2D finite-difference method and code (see previous chapter), efforts were made to seek exploitable geometries that would simplify the known 3D nature of the borehole environment into a 2D problem. Such exploitable geometries do exist.

Figure 3.1 shows a 3D volume (*x, y, z*) with a single dipping interface pierced by a vertical borehole and separating two layers of different acoustic impedances. No borehole-fluid effects are included in this representation and the media above and below the interface are isotropic. Receivers populate the borehole axis of the vertical borehole. A single source is located above the interface also along the borehole axis. Figure 3.1, shows the result of raytracing this model, as performed with the help of the NORSAR-3D™ modelling software. It illustrates the wavefield propagation in and around the borehole.

The results of the raytracing show that the reflected energy recorded at the receivers in the borehole is confined to the vertical plane subtended by the vertical borehole and the normal to the dipping interface. No other reflected energy from the dipping interface returns to the receiver arrays in the borehole and thus is never recorded. When the effects of the borehole fluid are added to the model (not shown here) the reflected energy recorded at the receivers is again propagating within this same vertical

plane, which also contains the direction of dip of the interface. From these results it can thus be shown, for simple single-well imaging geometries (Figure 3.1), that the 3D borehole problem can be simplified into a 2D problem by cutting the 3D volume with a vertical plane parallel to the dip direction of the interface and containing the vertical borehole path.
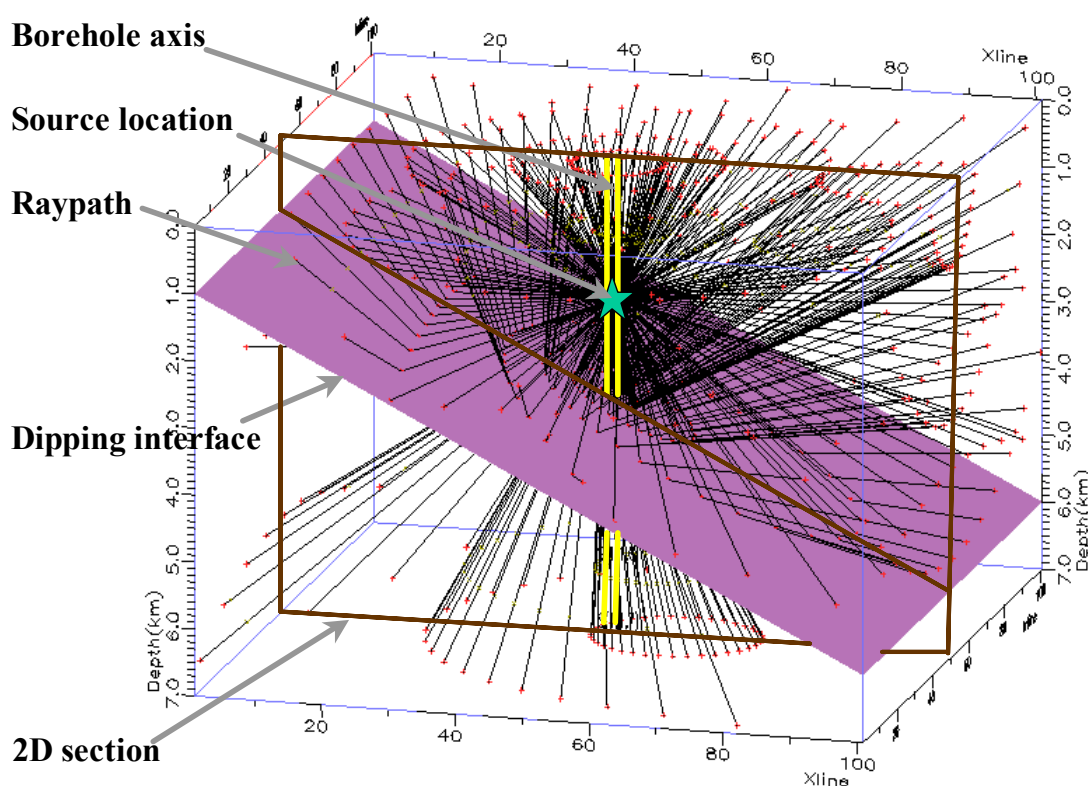
FIGURE 3.1. Raytracing of a simple 3D borehole model (*x, y, z*) with a dipping interface pierced by a vertical borehole. This view plots rays every 15° of azimuth and dip.

3.2   Creation of a synthetic dataset for a scatterer model

The model is two-dimensional, characterized by a vertical fluid layer confined on either side by identical elastic layers with one of the elastic layer having a scatter point embedded in it. A *scatter point* is a type of reflector that will reflect energy from any

source point on the borehole axis to any receiver point on the borehole axis. A more general reflector is composed from the superposition of appropriately positioned scatter points with each scatter point creating its own diffraction. The vertical fluid layer simulates the fluid-filled borehole. The finite-difference method and code introduced in the previous chapter were used to generate the synthetic traces.

A scale factor of 333 to 1 (modelled length to field length) was used to replicate the borehole environment in its main features. The model dimensions are similar to those introduced in Section 2.3. As shown in Figure 3.2, the borehole layer is filled with a fluid that has a compressional velocity, V_f, of 1500 m/s and a density, ρ_f, of 1000 kg/m^3. The medium located immediately on either side of the borehole fluid has a compressional velocity, V_{P1}, of 2600 m/s and a density, ρ_1, of 1700 kg/m^3. Finally, to capture the scatter point in the code, it was necessary to give it finite dimensions and acoustic impedances. This *scatterer*, or scatter point with finite properties, is of dimensions 20 m by 20 m (field 0.06 m by 0.06 m), has a compressional velocity, V_{P2}, of 3600 m/s and a density, ρ_2, of 5000 kg/m^3. Scatterers of different dimensions were tested before arresting the choice on the one with the above characteristics. Those tests were conducted in order to ensure that the scatterer would be small enough to behave as a true *scatter point* but yet large enough to have its energy captured by the receivers. Finally the model selected was an acoustic model (no shear wave enabled) in order to reduce the number of different borehole modes and simplifying the processing of the data.

A selected number of shot points were acquired, along the borehole axis, in the fluid-filled borehole. A total of five shot records were acquired. Those shots were located at 10, 750, 1250, 1500 m and at 1750 m (field at 0.03, 2.25, 3.75, 4.5 m and at 5.25 m)

along the borehole axis. Receivers were placed in a split-spread layout all along the borehole axis to record the particle velocity (both the z- and the x-components). A receiver spacing of 10 m (field 0.03 m) was used. The listening time at each receiver was 1600 ms (field 4.8 ms). Note that the well-logging tool is not accounted for in the model and thus the receivers essentially lie suspended in the fluid-filled borehole.
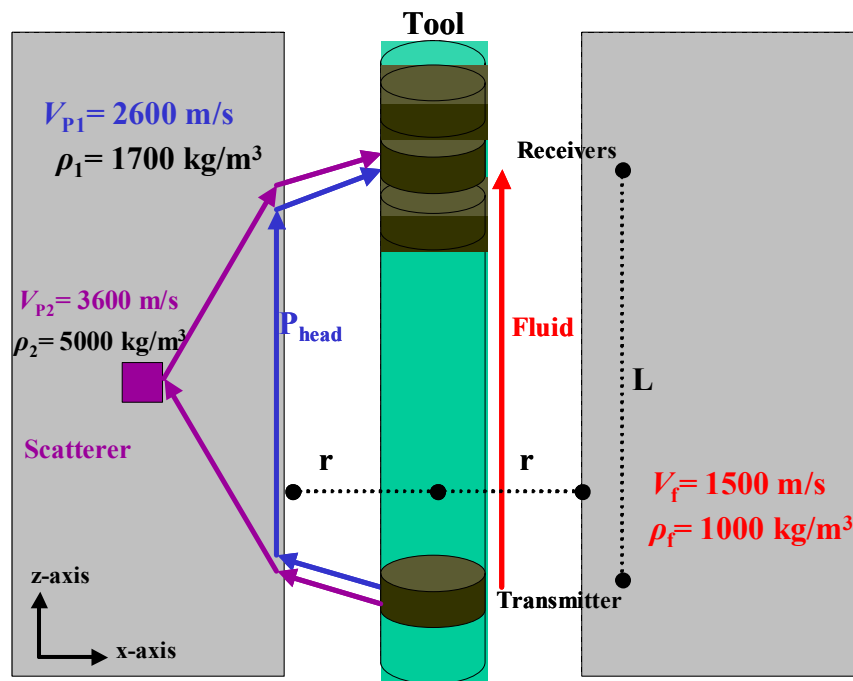
FIGURE 3.2. Diagram showing the borehole model with one scatterer. The radial distance axis is defined as the x-axis while the depth axis is defined as the z-axis. The scatterer is located in the borehole wall, halfway along the borehole model.

The wavefield generated by the finite-difference modelling calculation was saved in a series of snapshots at different times. These were plotted with the help of Matlab™. Figure 3.3 shows a sample snapshot of the wavefield at 700 ms (field 2.1 ms). Note that it took normally several hours to generate each shot record on an Ultra 60 Sun system.

The snapshot in Figure 3.3 displays the wavefield in the borehole fluid and in the surrounding formation at a time of 700 ms (field 2.1 ms) in two formats. The left portion

shows the vertical component (*z*-direction) of the wavefield while the right portion shows the horizontal component (*x*-direction) of the same wavefield. In this snapshot, the vertical or *z*-axis represents depth in metres in the borehole model, while the horizontal or *x*-axis represents radial distance perpendicular to the borehole axis in metres. Undisturbed borehole fluid and rock formation are represented as uniform grey. Components of particle velocity in the borehole fluid and formation are represented on a grey scale from white (negative) to black (positive) (normal polarity).
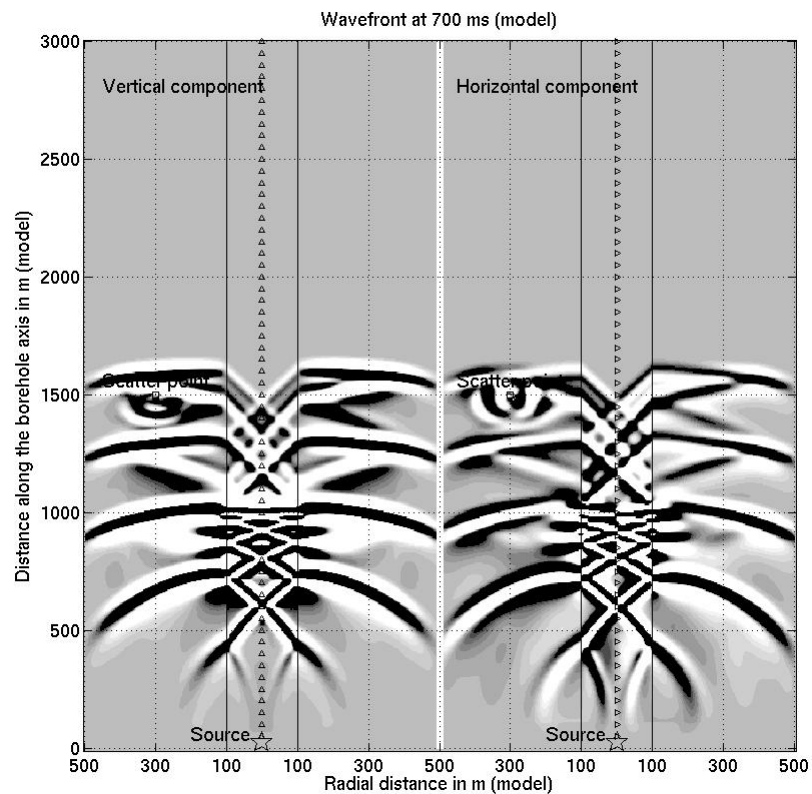
FIGURE 3.3. Snapshot of the wavefield at 700 ms (field 2.1 ms) generated by the finite-difference method. The source, polarized in the *z*-direction, was located in the fluid-filled borehole on the borehole axis at a distance of 30 m (field 0.09 m).

Again in reference to Figure 3.3, the generation of the direct P and the P head wave in the fluid can be observed. Behind the head wave in the borehole are the interface

waves such as the Stoneley wave. The guided borehole waves are generated from the source pulse in the borehole fluid, which is reflected from the formation many times. With each reflection, compressional waves are excited in the formation. Also, one can observe the evanescent nature of the Stoneley wave, which travels along the borehole wall more slowly than the fluid wave.
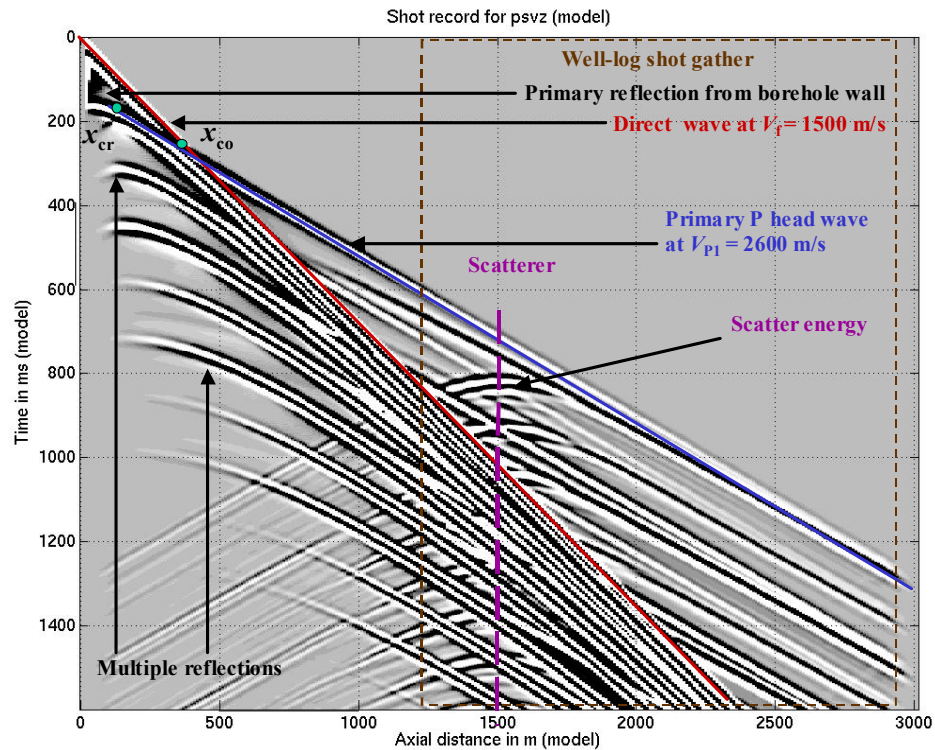
FIGURE 3.4. Common-shot gather recorded by the receivers on the borehole axis of the wave propagation in a fluid-filled borehole with a scatterer. Important events are labelled. Shown are model times and distances.

Figure 3.4 illustrates a shot record of the vertical component of particle velocity measured at the receivers along the borehole axis. This shot record represents a first approximation of the pressure field that would be recorded by borehole hydrophones. Note the complexity of the shot record. The following can be observed: the direct fluid wave (at 1500 m/s), the P reflection from the borehole wall, at $t_0 = 133$ ms (field 0.4 ms),

the P head wave (at 2600 m/s), and the interface-wave arrivals such as the Stoneley. Note also the strong presence of reverberations at t_0 = 266, 400, 533, 667 and at 800 ms (field at 0.8, 1.2, 1.6, 2.0 and at 2.4 ms) in the shot record. More importantly, notice the presence of the scattered energy in the shot record. This is the target signal for imaging.

The shot record obtained from this numerical simulation (Figure 3.4) has some undesirable effects when compared to actual waveform data acquired in the field. When comparing the two I noticed the absence of strong reverberations in the field data. This difference between the simulated and the field data full waveform could be accounted for by the difference between the 2D geometry of the model and the 3D geometry of the borehole environment. There were also reflections originating from the edges of the model appearing on the left side of the shot record created by the inadequate absorbing boundary. Finally, there is a 34 ms time delay for the onset of the arrival caused by the Ricker wavelet not starting at zero time.

The outputs were exported to ProMAX™ software where the waveform processing and imaging flow were tested.

3.3   Proposed processing-imaging flow for the scatterer model

3.3.1   Geometry and filtering

In processing the synthetic results, the first step consisted in assigning the appropriate geometry to the borehole environment. Thus, the z-coordinates along the borehole axis were transformed and translated from the original increasing numbering from the bottom to the top of the vertical borehole axis (Figure 3.3) into a decreasing numbering from the left to the right along the borehole axis that has become horizontal.

Next, I adopted the convention that, for receivers located to the left of the shot, offsets are negative and, for receivers located to the right of the shot, offsets are positive. The result of the application of this convention is shown in Figure 3.5.
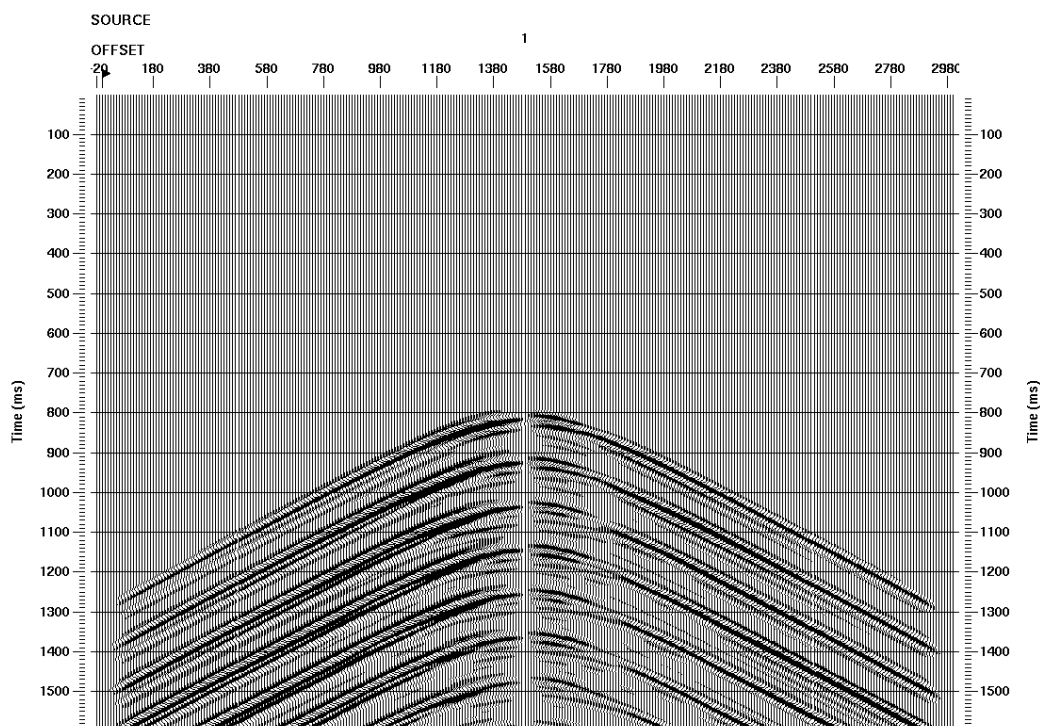
FIGURE 3.5. Difference shot record acquired along the borehole axis. Note the presence in this shot record of only the P scattered energy. The reverberations in the borehole generate the observed multiples. The shot location is represented by a small flag.

To recover the scattered energy present in the shot records, the interface waves and the reflections from the edge of the model were filtered out by subtracting the shot record generated without the scatterer present (homogeneous case) from the original shot record that contained the effect of the scatterer (non-homogeneous case). Although this filtering technique cannot be applied to field data, it is an approach that ensured that I recovered the scattered energy. Thus, this 'optimal' filtering technique was applied to all

five simulated shot records to produce the filtered synthetic acoustic dataset, an example of which can be seen in Figure 3.5.

3.3.2 Introduction to the concept of equivalent-offset migration (EOM)

Equivalent-offset migration (EOM) is a prestack time migration made up of several steps (Bancroft *et al.*, 1998). The first step consists of forming prestack migration gathers called common-scatter-point (CSP) gathers from the input traces. The CSP gathers are generated by mapping input traces to an equivalent offset, h_e. This step is followed by a focusing process that applies a simplified Kirchhoff migration to the CSP gathers, involving scaling, filtering and normal-moveout (NMO) correction. The final step consists in stacking the 'corrected' gathers. The objective of this prestack time migration is to collect all the scattered energy and relocate it to the position of the scatter point.

A scatter-point impulse response in the prestack volume (*x, h, t*) yields a traveltime surface called a Cheops pyramid (Claerbout, 1984). Equation (3.1) is the reformulation of the double-square-root equation and provides the relations needed to map the traces from the seismogram, one to one, in a CSP gather. In equation (3.1): h_{cmp} is the distance from the CMP location of the input trace to the CSP; h is the half source-receiver offset; T_t is the recorded time, and T_α, is the first useful sample in time of a trace on the CMP to be mapped to a fixed offset bin in the CSP gather. In general, a CSP gather taken at the scatter-point location will yield a hyperbola of the form:

$$h_e^2 = h_{cmp}{}^2 + h^2 - \left(\frac{2\ h_{cmp}\ h}{T_t\ V_{mig}} \right)^2 \qquad (3.1)$$

$$h_{cmp} = \frac{V_{rms} \, T_\alpha}{2} \qquad (3.2)$$

$$\text{and} \quad V_{mig} = V_{rms} = \sqrt{\frac{t_1 \, V_{P1}^2 + t_f \, V_f^2}{T_t}} \, . \qquad (3.3)$$

The EOM was selected as the preferred method of imaging in this work because a CSP gather has a higher fold and a larger offset range than a common-midpoint (CMP) gather and thus is more likely to contain coherent scattered energy from a scattering point. In other words, the maximum equivalent offset of the CSP gather is equal to the migration aperture and is much larger than the maximum source-receiver offset of the CMP gathers. The creation of CSP gathers is fast because no time shifting, scaling or filtering is involved. Finally, EOM has been successfully used not only to image regular seismic data but also to image vertical-array data (Bancroft and Xu, 1999).

3.3.3   Imaging of the scatterer by EOM

Common-scatter-point (CSP) gathers were formed using a binning size of 5 m (field 0.02 m) with a migration aperture of a maximum of 1250 m (field 3.75 m). The selection of the migration aperture is important because it is the spatial envelope of each trace that will contribute to the focusing of the scattered energy. The result of the application of this first step of EOM to the synthetic dataset is presented in Figure 3.6 with the one-sided CSP gather format at the scatterer location or at CSP 304.
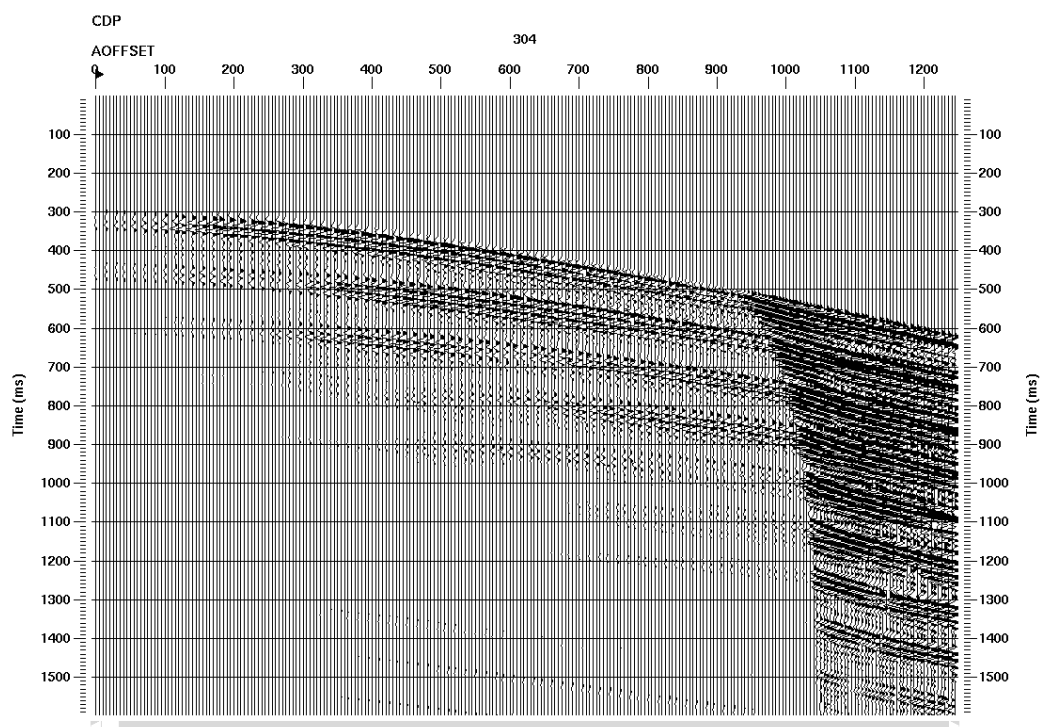
FIGURE 3.6. One-sided CSP gather of the synthetic acoustic data at CSP number 304. This CSP number coincides with the location of the scatterer.

It is important to note (Figure 3.6) that although the primary reflection from the scatterer has a stacking velocity of 2160 m/s (theoretical root-mean-square or RMS velocity), the multiples of the scatterer, arriving at later times, have progressively slower stacking velocity starting at 1976 m/s and decreasing. This velocity profile can be explained by the increase in traveltime in the fluid.

Once the CSP gathers were formed, the next step in the EOM method consisted in applying NMO correction to the individual CSP gathers. The velocity value selected for the proper application of the NMO to the synthetic dataset corresponded to the calculated RMS velocity of the model using equation (3.3) or 2160 m/s. NMO used a 50% stretch mute. Once this step was completed, a straight stack was applied to the NMO-corrected data to generate the final image in time. This final image is shown in Figure 3.7.
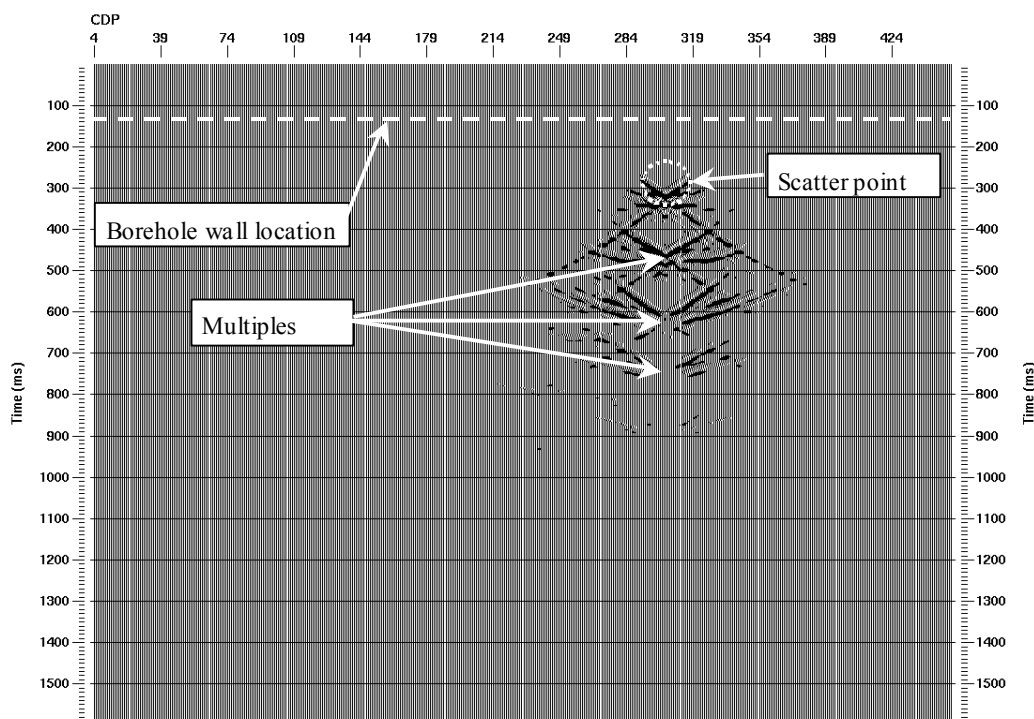
FIGURE 3.7. The energy from the scatter point is focused at approximately CSP number 304 and at 310 ms (field 0.93 ms) (circled by a white dashed line).

The location of the scatter-point image (Figure 3.7) closely corresponds to the predicted position of the scatter point at CSP 304 and 287 ms (field 0.86 ms). Note that, because of the multiple energy created by the reverberations, predominantly between the borehole wall and the scatter point, there are several multiples of the scatter point present later in time at 440, 595 and 750 ms (field 1.32, 1.79 and 2.25 ms). Those events are not imaged properly because of the selected stacking velocity being higher than the stacking velocities of those individual multiples.

3.4   Creation of a synthetic dipping interface dataset

The model is two-dimensional, characterized by a vertical fluid layer confined on either side by elastic layers cut by a dipping interface, where the properties above the

interface are different than those below the interface. The vertical fluid layer simulates the fluid-filled borehole (Figure 3.8).

A scale factor of 333 to 1 (modelled length to field length) for lengths was used to replicate the borehole environment in its main features. The model dimensions are similar to those introduced in Section 2.3. As shown in Figure 3.8, the borehole layer is filled with a fluid that has a compressional velocity, V_f, of 1500 m/s and a density, ρ_f, of 1000 kg/m³. The medium located immediately above the interface, on either side of the borehole fluid, has a compressional velocity, V_{P2}, of 2500 m/s and a density, ρ_2, of 2000 kg/m³. The medium located immediately below the interface, on either side of the borehole fluid, have a compressional velocity, V_{P1}, of 3500 m/s and a density, ρ_1, of 2000 kg/m³. The dipping interface makes an angle of 33.6 degrees with the borehole axis.
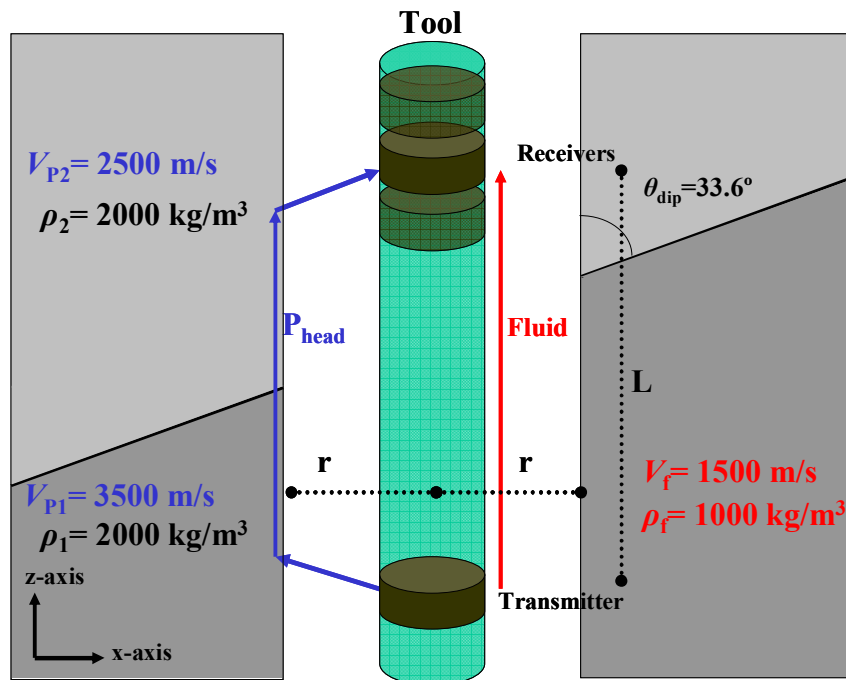
FIGURE 3.8. Diagram showing the borehole model with one dipping interface.

Because the finite-difference method could not be used to create such a model, a 2D raytracing method by NORSAR™ was used instead to generate the synthetic data. The smallest possible programmable dimension in NORSAR™ is 1 m (length and width). Finally the model selected was an acoustic model (no shear wave enabled) in order to reduce the number of different borehole modes and simplifying the processing of the data.

For the imaging experiment, a total of sixteen shot records, at a nominal spacing of 150 m (field 0.45 m), were acquired along the vertical borehole axis from 0 to 2250 m (field 0 to 6.75 m). Receivers were placed along the borehole axis to record the arrival time. Unlike the previous models, an end-spread layout with a receiver spacing of 50 m (field 0.15 m) was used with a near offset of 0 m and a far offset of 750 m (field 0 to 2.25 m). The listening time at each receiver was 1000 ms (field 3 ms). Note that the well-logging tool is not accounted for in the model and thus the receivers lie suspended in the fluid-filled borehole.

The rays generated by the raytracing calculation were accumulated and superimposed into a composite display with all sixteen shots (Figure 3.9). In this display, the vertical or z-axis represents depth in kilometres in the borehole model, while the horizontal or x-axis represents radial distance perpendicular to the borehole axis in kilometres. This display shows that the successful reflected energy originates exclusively either from the downdip portion of the interface (relative to the well), when the well-logging tool is below the interface, or from the updip portion of the interface (relative to the well) when the well-logging tool is above the interface. As will be seen later, this observation is critical for the further processing of the data.
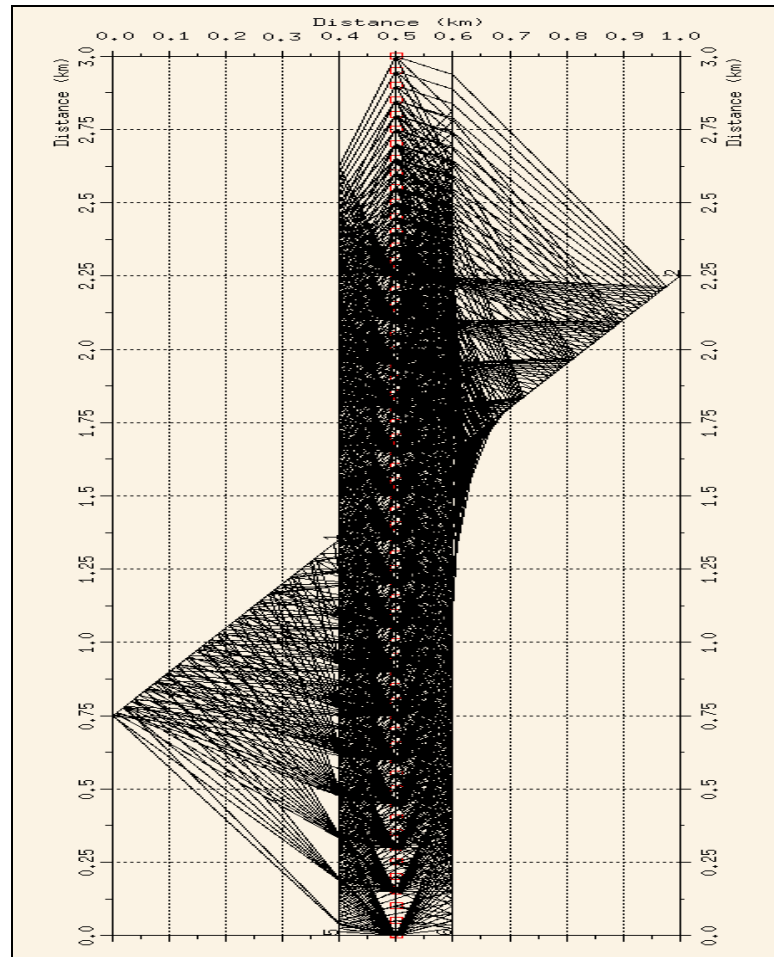
FIGURE 3.9. Cumulative raytracing for 16 shots generated by the raytracing method. The source was located in the fluid-filled borehole on the borehole axis (shown are model dimensions).

The individual shot records were next superimposed, as shown in Figure 3.10, into a composite display for all sixteen shots using the same z-axis reference as in Figure 3.9. This display shows with a tick mark the individual arrival times of the various borehole modes enabled: the direct fluid wave with a linear moveout at 1500 m/s (repeated in all shot records) labelled as "dirP", the primary reflection from the borehole wall at $t_0 = 133$ ms (field 0.4 ms) and its first multiple at $t_0 = 266$ ms (field 0.8 ms) (repeated in all shot records) labelled as "multiples_1", the reflections from the downdip

portion of the interface (broad hyperbolas moving up in time as the source-receiver arrays moves uphole and approaches the interface) labelled as "P_r1_P" and the reflections from the updip portion of the interface (narrow hyperbolas moving down in time as the source-receiver arrays continues to moves uphole but away from the interface) labelled as "P_r2_P". This behaviour is shown schematically in Figure 3.11. The reflected energies in the shot records are my target signals for imaging.
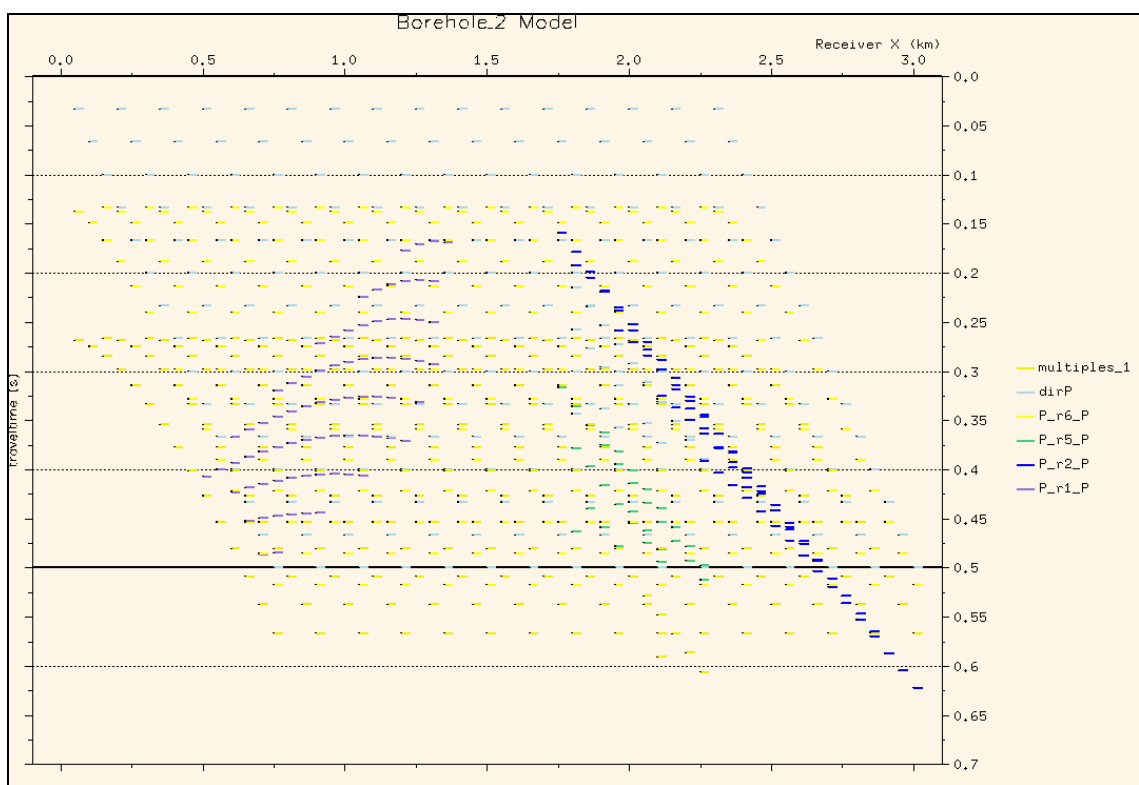
FIGURE 3.10. Superimposed common-shot gather recorded by the receivers on the borehole axis of the wave propagation in a fluid-filled borehole with a dipping interface. Shown are model times and distances.

The traveltime outputs were convolved with a 30-Hz Ricker wavelet and were exported to ProMAX™ where the waveform processing and imaging flow were tested.

Full waveform Data set

**Time contours of
Cheops pyramid**

h

**Vertical plane of
Source records**

Scatter point

**Dipping prestack surface
(downdip in the borehole)**

**Dipping prestack surface
(updip in the borehole)**
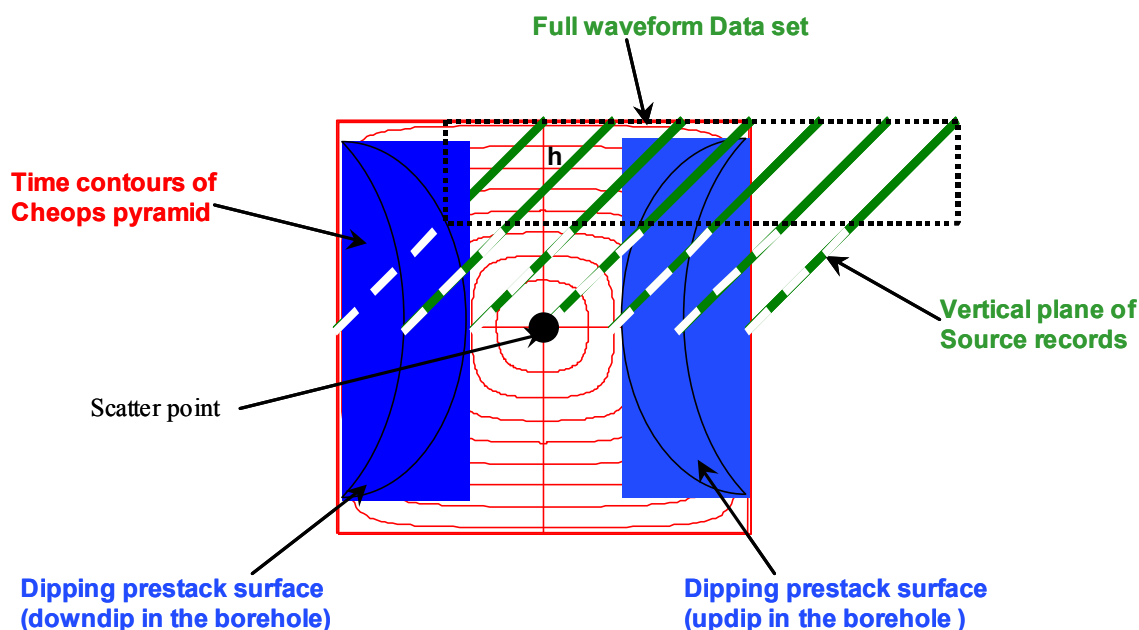
FIGURE 3.11. Plan view of the two dipping prestack surfaces in the prestack volume (*x*, *h*, *t*), for 2D data with all four quadrants (positive and negative offsets, *h*).

3.5 Proposed processing-imaging flow for the synthetic dipping interface dataset

3.5.1 Geometry and filtering

In processing the synthetic results, the first step consisted in assigning the appropriate geometry for the borehole environment. This procedure was similar to the one described in Section 3.3.1. Figure 3.12 shows shot record number 16 acquired in the top most portion of the borehole where the direct fluid wave, the primary reflection from the borehole wall and its first multiple and the reflection from the updip portion of the interface can be identified. It is important to note that the amplitude of the reflection from the interface is of markedly smaller magnitude than either the direct or the reflected arrivals from the borehole wall.
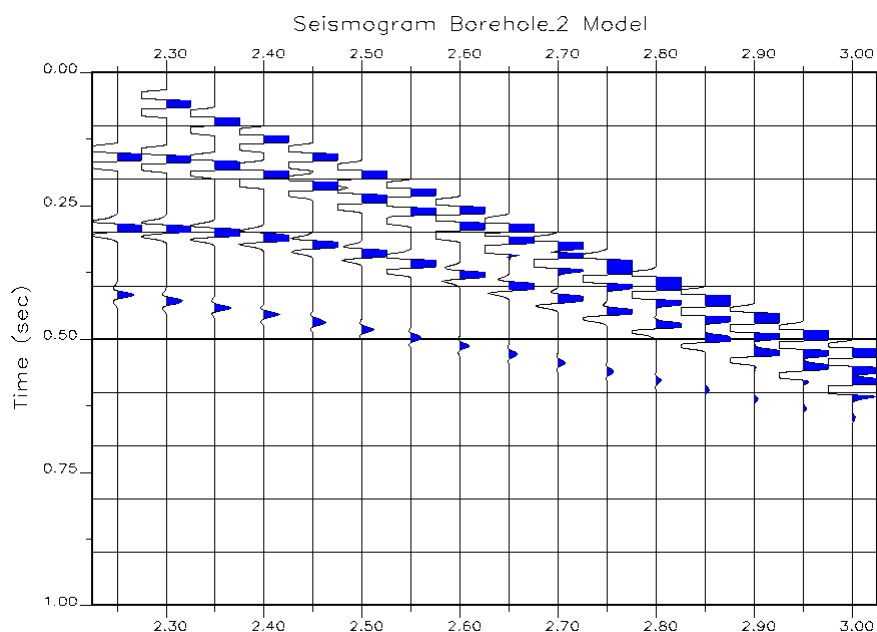
FIGURE 3.12. Shot record number 16 acquired in the uppermost part of the borehole showing the different events recorded: the direct fluid wave, the reflection from the borehole wall and its multiple and the reflection from the interface.

To maximize the quality of the final migrated image, and thus help validate the proposed imaging process, the direct fluid wave and the reflections from the borehole wall were disallowed in the raytracing in all of the sixteen shot records before processing. This action was taken to minimize the presence of artifacts that would have been generated by the filtering step and thus degrade the quality of the final migrated image. Thus, this approach, equivalent to an 'optimal' filtering step, was selected for all sixteen simulated shot records to produce the synthetic acoustic dataset.

3.5.2   Imaging of the dipping interface by EOM

The focusing and imaging of the filtered synthetic data were next done with the use of the equivalent-offset migration (EOM). Unlike what was done in section 3.3.3, two-sided gathers were used instead, where one side contains the negative equivalent

offsets and the other the positive equivalent offsets. Two-sided CSP gathers have the advantage of making it possible to see how the contributions from different azimuths differ from each other and thus how linear, diffracted, and dipping events can be better distinguished. In this case, common-scatter-point (CSP) two-sided gathers were formed using a binning size of 25 m (field 0.08 m) with a migration aperture of a maximum of 750 m (field 2.25 m). The selection of the migration aperture is important because it is the spatial envelope of each trace that will contribute to the focusing of the scattered energy. In other words, the CSP gather is composed of all input traces within the prestack-migration aperture. The result of the application of this first step of EOM to the synthetic dataset is presented in Figure 3.13.

The newly formed two-sided CSP gathers were next split and sorted into two separate families of one-sided gathers. The CSP gathers with negative equivalent offsets, were arranged together representing the updip portion of the interface crossing the borehole, while those with positive equivalent offsets, were arranged together representing the downdip portion of the interface crossing the borehole. Once this separation was completed, I applied NMO (50% stretch mute) with the correct velocity profile to the CSP gathers with the negative equivalent offsets, followed by a conventional stack, thus creating the prestack time-migrate image of the updip region of the hole. I also applied NMO (50% stretch mute) with the same velocity function to the family of CSP gathers with the positive equivalent offsets, followed by a conventional stack, thus creating the prestack time-migrate image of the downdip region of the hole. The two processed sections were next combined along their common zero time, which in

the final image becomes the well axis. The final processing results are presented in a composite image in Figures 3.14.
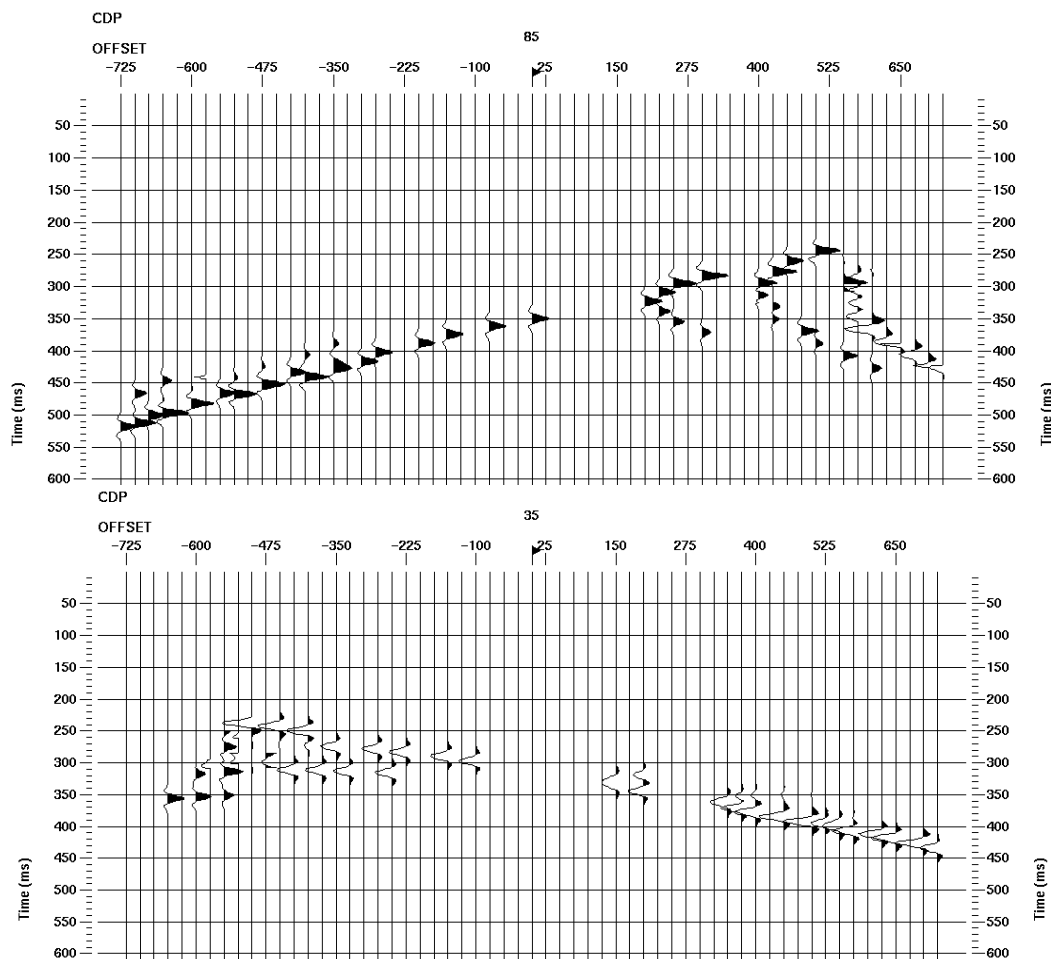
FIGURE 3.13. Two-sided CSP gather of the synthetic acoustic data at CSP number 35 (lower part of the borehole) and 85 (upper part of the borehole) (truncated to 600 ms).

The location of the dipping interface image, in Figure 3.14, closely corresponds to the predicted position of the dipping interface at the borehole wall at CSP 56 at 133 ms (field 0.4 ms) in the downdip side and at CSP 66 and 133 ms (field 0.4 ms) in the updip side.

The downdip portion of the interface is shown as a trough because it represents change in acoustic impedance from hard to soft, while the updip portion of the interface

is shown as a peak because it represents a change in acoustic impedance from soft to hard. The borehole outline is represented by the vertical dashed lines. There is also the presence of processing artifacts in the final composite image, highlighted by the dashed ellipses, with the smearing of energy. Those observations will be critical in properly interpreting the composite sonic image of the field data presented in Chapter 5.
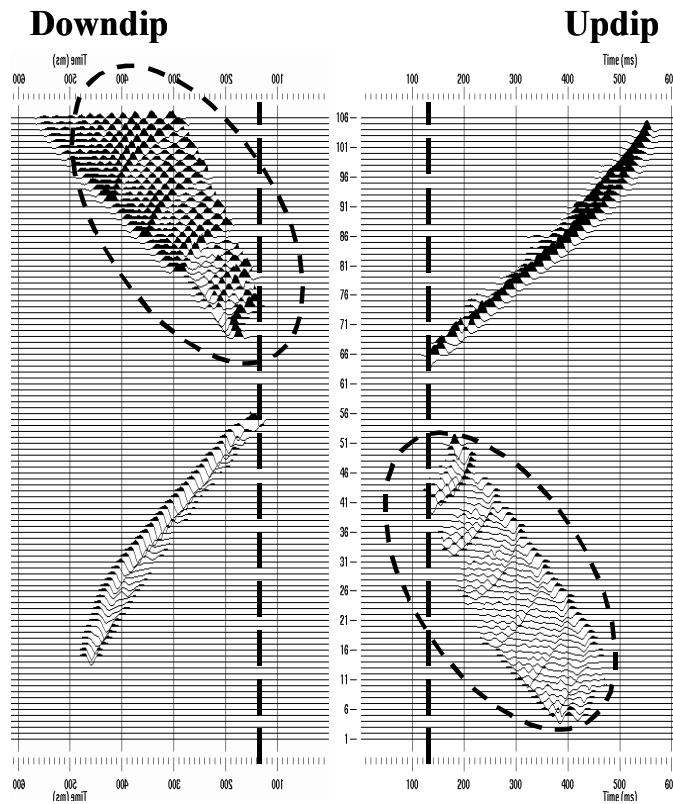
FIGURE 3.14. The energy from the dipping interface is focused at approximately CSP number 30 and 65 (see dipping line). Shown are model times and distances.

CHAPTER 4: FULL-WAVEFORM SONIC FIELD DATA

4.1   Location of field data

The full-waveform field dataset studied here was acquired in the open-hole section of the 8-8-23-23W4 well located in the Blackfoot field in Alberta (see Figure 4.1). The geology of the Blackfoot field is summarized by Miller *et al.* (1995).
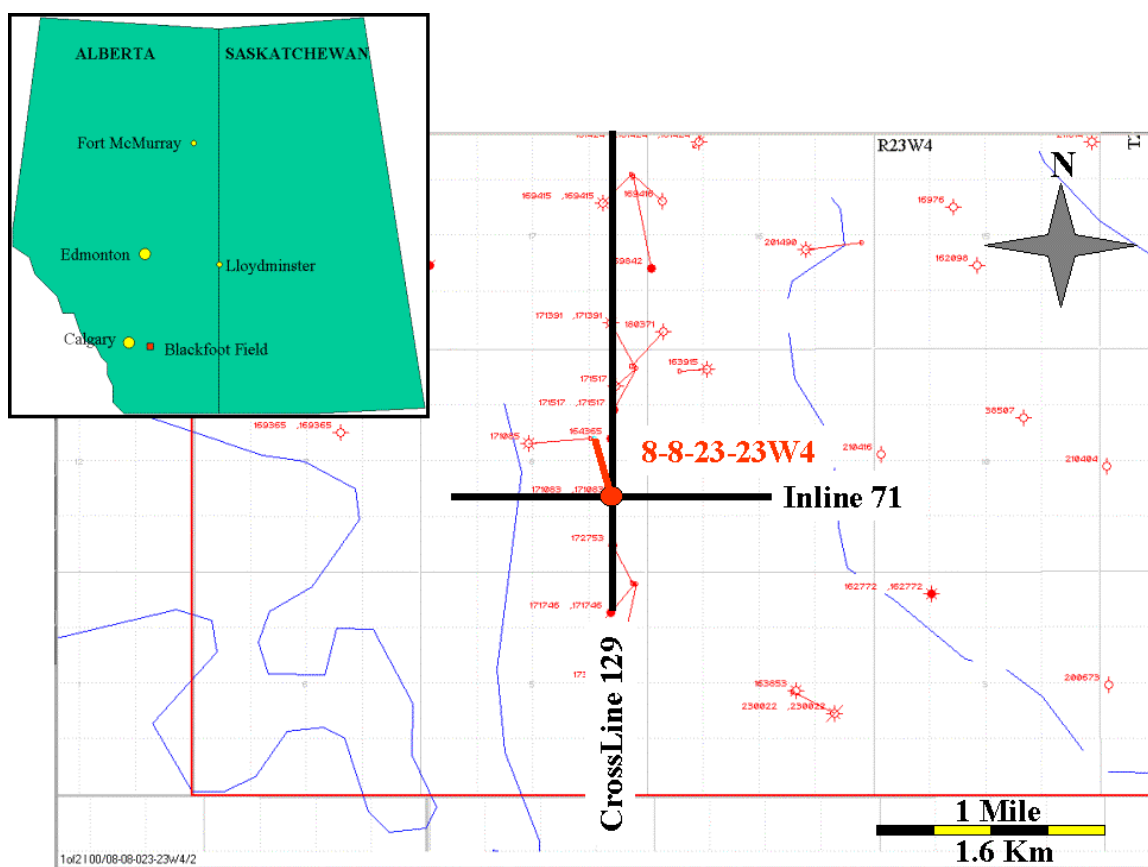
FIGURE 4.1. Surface location of the 08-08-23-23W4 well in the Blackfoot field.

4.2   Well-log data and sonic tool geometry

This dataset consists of 310 m of full-waveform data, acquired in the deviated section of the well. This deviated section of the well oriented at an angle of 20° to 30° from the vertical intersects a flat-lying sequence of alternating sandstones, shales and

limestones from the top of the Mannville group to the Mississippian unconformity. The hole-orientation data (azimuth, deviation and depth) was absent from this well and had to be estimated. This was done using the well top and bottom UTM coordinates and from the measured and true vertical formation-top depths provided.

The full-waveform data were acquired with a DSI™ (Figure 4.2), a conventional well-logging tool, in a monopole configuration, with an acoustic bandwidth of 8 to 30 kHz. Eight receivers were located 15 cm apart on the tool with a near-offset distance to the source of 2.74 m and a far offset of 3.81 m. The well-logging tool has a diameter of 92.1 mm. Eight full waveforms were recorded simultaneously at the firing of the monopole source to create a shot gather. Each waveform was recorded at a sampling interval of 10 ms for a total of 512 samples/waveform (Harrison *et al.*, 1990).
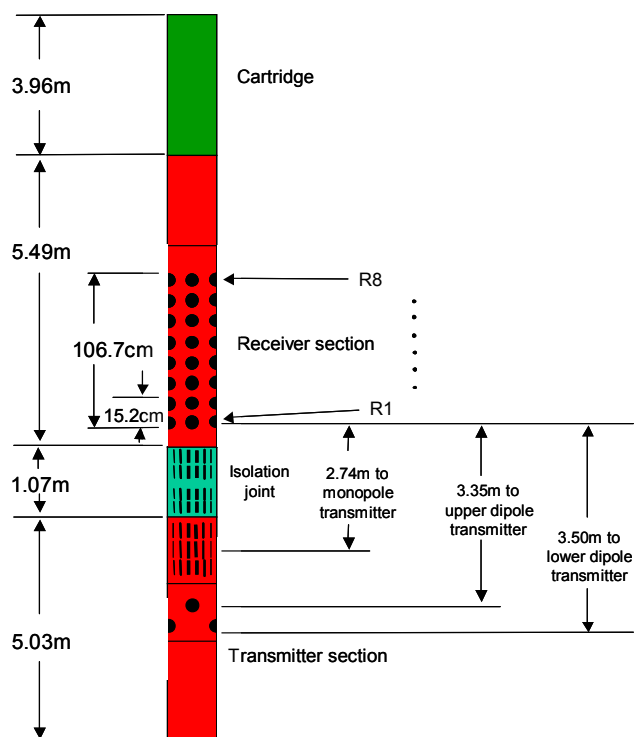
FIGURE 4.2. Diagram representing the tool geometry of the DSI™ acoustic well-logging tool (modified after Schlumberger, 1997).

The full waveforms are normally processed to output P and S velocities. Those P and S velocities are referenced to a measure point that lies between the fourth and fifth receivers of the DSI™. This translates into a distance from source to measure-point of 3.28 m. This distance is important in comparing the full-waveform processing results with the conventional acoustic well-log data.

4.3   Full-waveform dataset

Figure 4.3 illustrates a sample of five consecutive shot gathers, of eight full waveforms each, taken from source depths of 1631.37 m to 1630.76 m in the well. A look at Figure 4.3 reveals the presence in the full waveforms of the compressional (4445 m/s), shear and pseudo-Rayleigh (2481 m/s), fluid or direct (1560 m/s) and Stoneley (1404 m/s) arrivals, all of which have linear moveout. These waveforms could also contain energy scattered from beyond the borehole wall.
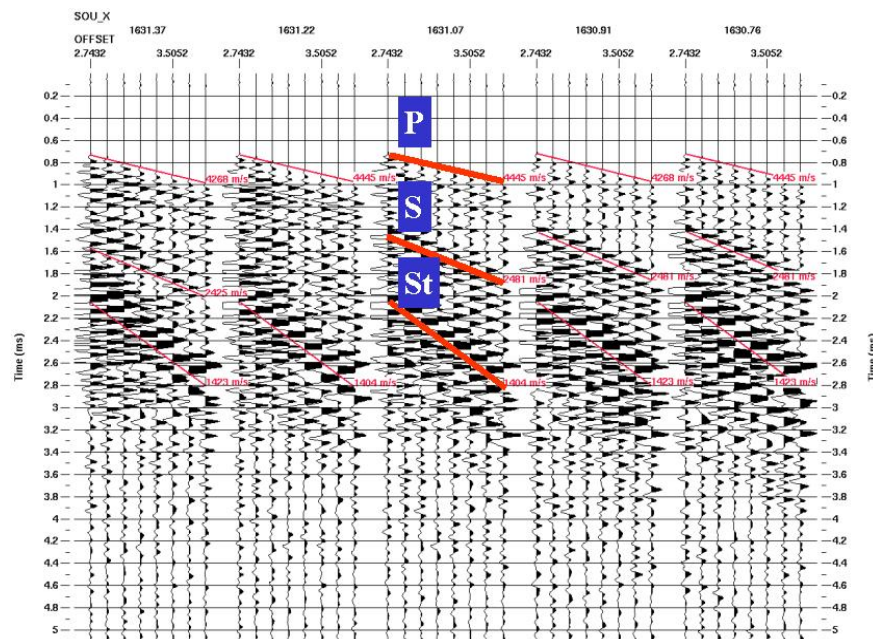
FIGURE 4.3. Identification of compressional (P), shear and pseudo-Rayleigh (S) and Stoneley (St) arrivals in a sample of five sonic shot gathers; vertical scale in ms.

However, as can be seen in these raw shot records, because the energy with the linear moveout is so more prominent than the energy from reflections, it will make interpretation in the present form difficult.

4.4   Characteristics of the full-waveform field data

The frequency spectrum of the full waveform has generally a multipeaked appearance, with a series of alternate peaks and troughs. Figure 4.4 shows a typical frequency spectrum of the full-waveform field data where the upper left side displays the raw full-waveform data, the lower left side displays the corresponding frequency spectrum, while the right side displays the average frequency spectrum for all 40 traces.

The peaks in the frequency spectrum can be interpreted in the following way: the low relative amplitudes at frequencies from 15 to 21 kHz, approximately, represents the P-wave; the intermediate relative amplitudes at frequencies from 8 to 11 kHz, approximately, represents the shear and pseudo-Rayleigh waves, while the high relative amplitude at frequencies from 5.5 to 7 kHz, approximately, represent the Stoneley wave. The troughs in the frequency spectrum probably correspond to the cut-off frequencies for the different normal modes. Given a temporal sampling of 10 μs for the full-waveform, the Nyquist frequency is at 50 kHz. Note that in Figure 4.4, frequencies are shown to 26 kHz only. The frequency spectrum of the full-waveform is affected at other locations in the borehole by the compressional and shear velocities of the formation, borehole diameter and borehole-fluid velocity (Tsang and Rader, 1979).
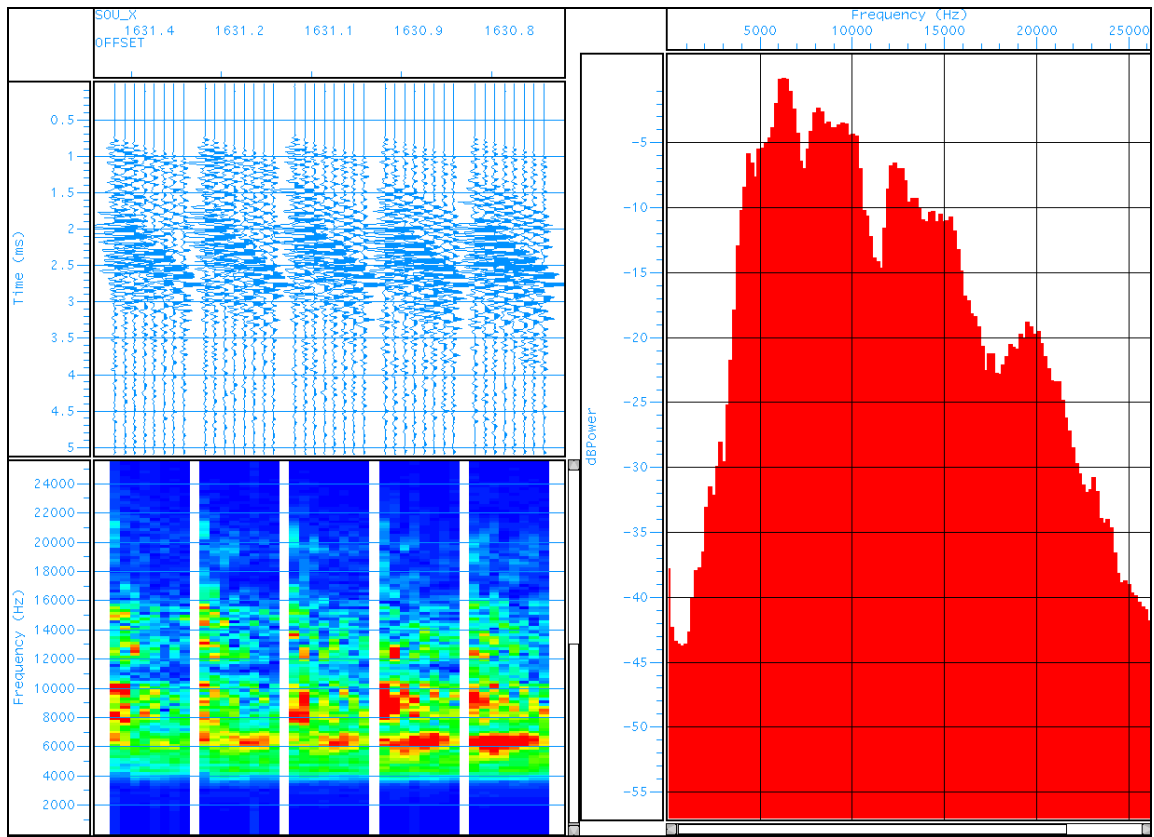
FIGURE 4.4. Frequency content of the full waveform; analysis done on the same five waveforms as shown in Figure 4.3.

Figure 4.5 shows a typical 2D *f-k* transform where the left side displays the raw full waveform, while the right side displays the computations of the wavenumber and frequency components of that full waveform. In the right side display of Figure 4.5, the horizontal scale is the wavenumber axis *k* while the vertical scale is the frequency axis *f* up to a maximum of 26 kHz. The apparent velocities, V_a, in the time domain can be related to the velocities in the *f-k* domain though the application of equation 4.1.

$$V_a = \frac{\Delta x}{\Delta t} \quad \text{and} \quad V_a = \frac{\Delta f}{\Delta k} \tag{4.1}$$

Given a spatial sample rate of $\Delta x = 0.15$ m and an apparent velocity V_a, then there will be spatial aliasing for all temporal frequencies higher than the critical frequency f_c, given by:

$$f_c = \frac{V_a}{2\,\Delta x} \qquad (4.2)$$

The 2D f-k transform of the full waveform generally displays spatial aliasing. For the example in Figure 4.5, f_c is 4.68 kHz for the Stoneley wave, f_c is 8.3 kHz for the S-wave pseudo-Rayleigh waves and f_c is 14.8 kHz for the P-wave. Spatial aliasing is present in all the wave modes. This will have an impact on the choice of the filtering method.
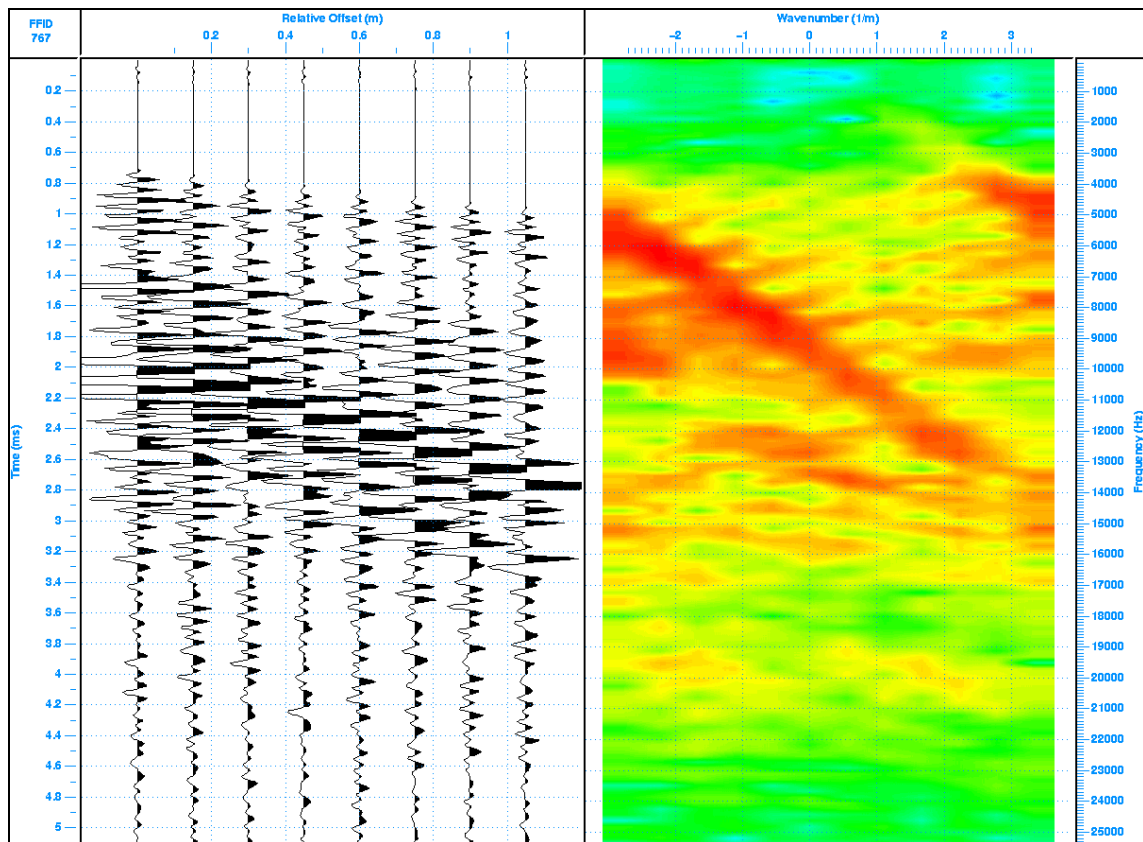
FIGURE 4.5. 2D f-k transform of the full-waveform middle shot record in Figure 4.3.

4.5   Common-offset sonic section

Prior to processing the full waveform into an image it is important to analyze further the raw full-waveform field data. The analysis of the raw full waveform data can best be achieved by displaying the raw full-waveform data in a single-receiver constant-offset variable-density plot also called a common-offset sonic section. In this case a constant transmitter-to-receiver spacing of 3.05 m was selected. In this display format (see Figures 4.6 to 4.9) the onset times, the relative attenuations of the different modes and as well as different interference patterns can best be observed.

Figures 4.6 to 4.9 show, from left to right, in the first track the formation tops, in the second track the gamma-ray log on a scale from 140 to 0 API, in the third track the compressional velocity log, V_P, on a scale of 7000 to 2000 m/s, in the fourth track the shear-velocity log, V_S, on a scale from 3400 to 1600 m/s, in the fifth track the caliper log (hole diameter) on a scale of 100 to 300 mm and in the last track, over the same depth interval, the corresponding full-waveform common-offset sonic section (at 3.05 m) from 0.5 to 4 ms (truncated). The common-offset sonic section is labelled for the onset of the compressional (P_{head}), shear-pseudo-Rayleigh (S_{head}) and Stoneley waves (St).

The onset times of the various borehole modes, keeping the borehole diameter relatively constant, can be used as an indirect identification of lithology. For example, the Pekisko limestone is identified by the earliest onset compressional time of 0.6 ms (Figure 4.9), while the shales (0.9 ms) can be distinguished from the sands (0.8 ms) by late arriving compressional onsets. In addition, as the S-wave velocity of the formation approaches that of the drilling mud velocity of 1500 m/s (approximately), the shear-pseudo-Rayleigh modes disappear from the waveform log (Figure 4.6). Note at the

bottom of Figure 4.7 the presence of a spike in both the V_P and V_S log, at 1574 m, which is not present in the corresponding common-offset sonic section. This spike in the logs is an artifact of the processing of the full waveform, probably caused by the selection of an improper fixed-length time window for the slowness-time-coherence processing (Schlumberger, 1997), and is not an indication of true rock lithology.

Compressional, shear pseudo-Rayleigh and Stoneley modes attenuation, in the sonic full-waveform, can provide another source of information about the characteristics of the rocks surrounding the borehole, assuming a non-rugose hole and a hole of constant cross-section (no washout). According to Dennis *et al.*, (1987) compressional and shear attenuation indicates both the presence of porosity and fractures in the formation. However in reservoirs where the porosity varies greatly, it may be difficult to distinguish between the two effects. Also, according to Dennis (1985) and Morris *et al.* (1964) the compressional and shear modes in the sonic waveforms also attenuate differently and independently, depending at which angle the fracture plane, when present, crosses the borehole. For example, the preferential attenuation of the shear pseudo-Rayleigh modes versus the compressional mode may be indicative of a fracture plane crossing the borehole axis at an angle between 90° (perpendicular to the axis of the borehole) and 60°.

Looking at the full-waveform field data it is difficult to say with certainty the impact that porosity and fractures have on the attenuation of the full-waveform data. However it can be surmised that in the carbonate section (Figure 4.9) no fractures are present given the low porosity of that section and the lack of attenuation of the compressional and the shear pseudo-Rayleigh modes. In addition there is no apparent attenuation of the Stoneley wave in that carbonate zone. On the other hand, in the

common-offset sonic section in Figure 4.8 it can be noted that the shear and Stoneley waves are strongly attenuated in the vicinity of the three coal seams, but not the compressional waves. This could be indicative that the angle between the three coal surfaces and the borehole axis could lie between 90° (perpendicular) and 60°.

In the common-offset sonic section, observed interference patterns may be caused by mode conversion, fractures and reflections from bed boundaries (Jorden and Campbell 1986). For example, interference patterns across a bedding plane or other discontinuity can be observed as V-and W-shaped patterns (Basick, 1983). Reflections generated when the borehole Stoneley wave encounters a permeable fracture or a major lithology change shows as a V-shaped pattern for a single-receiver, common-offset plot where the Stoneley wave reflected arrivals have an apparent moveout of $2\Delta t_{St}$ (Hornby *et al.*, 1987).
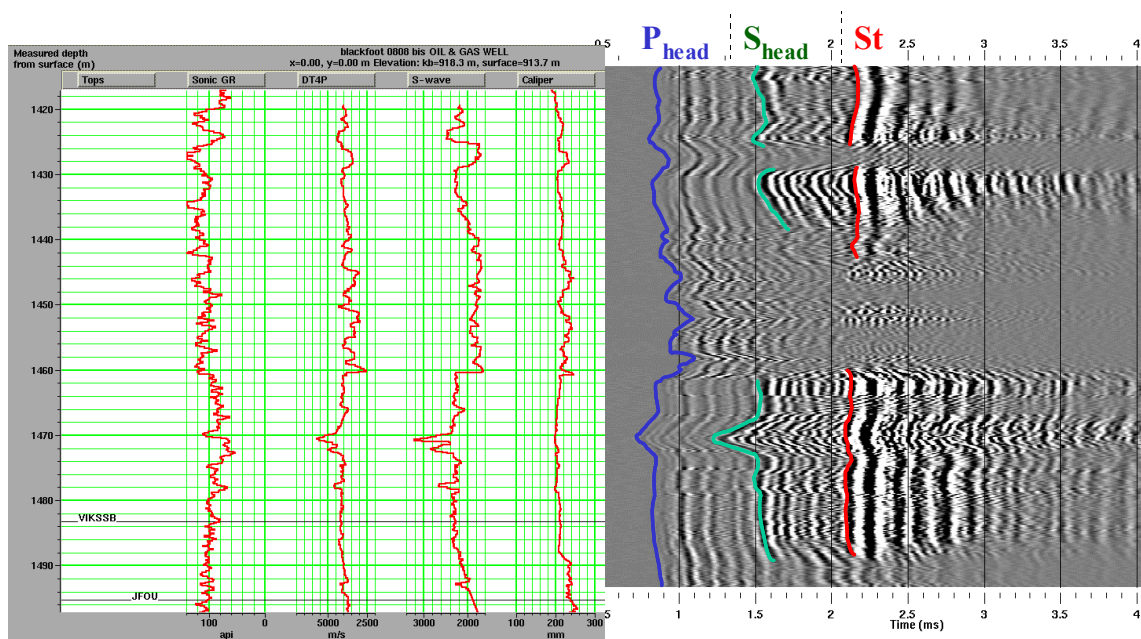
FIGURE 4.6. Open-hole well logs (left) and the corresponding full-waveform common-offset sonic section (at 3.05 m) from 0.5 to 4 ms over the depth interval of 1420 m to 1495 m. Formation tops present over the interval are Viking sandstone (VIKSSB), and Joli Fou shale (JFOU).
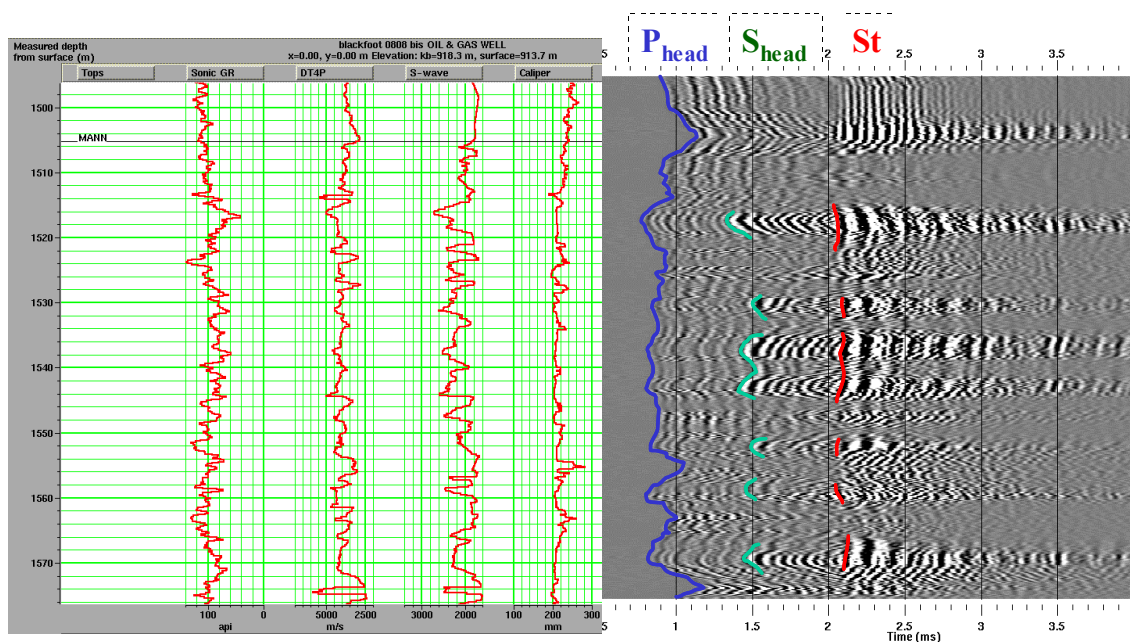
FIGURE 4.7. Open-hole well logs (left) and the corresponding full-waveform common-offset sonic section (at 3.05 m) from 0.5 to 4 ms over the depth interval of 1495 m to 1575 m. Formation top present over the interval is the Mannville (MANN).
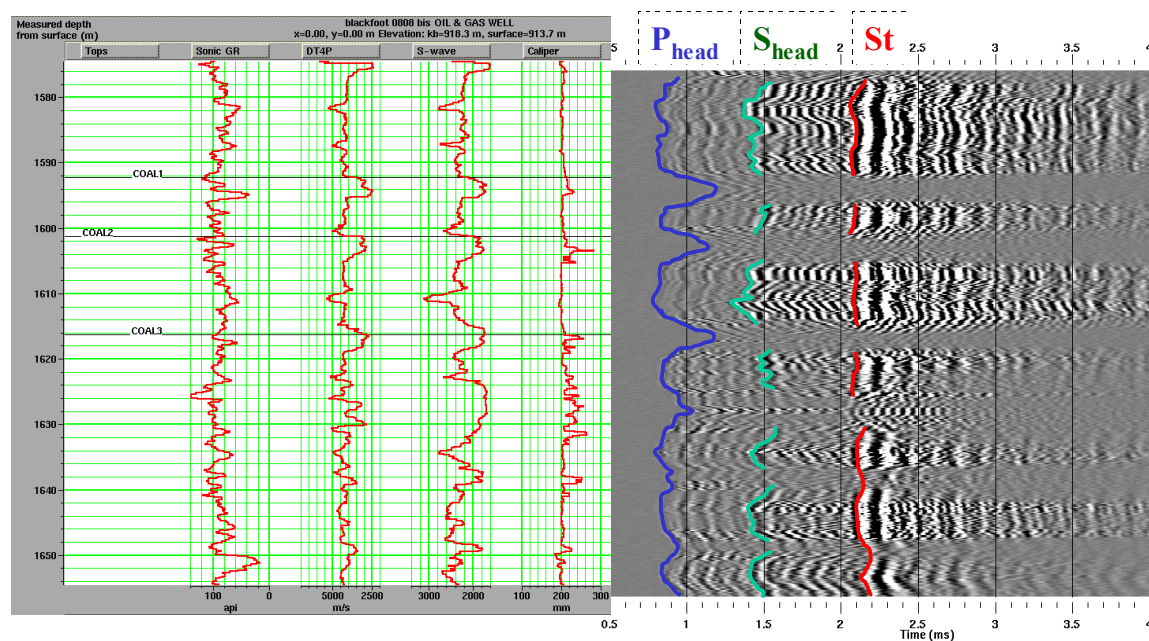
FIGURE 4.8. Open-hole well logs (left) and the corresponding full-waveform common-offset sonic section (at 3.05 m) from 0.5 to 4 ms over the depth interval of 1575 m to 1655 m. Formation tops present over the interval are three coal seams (COAL 1, 2 and 3).
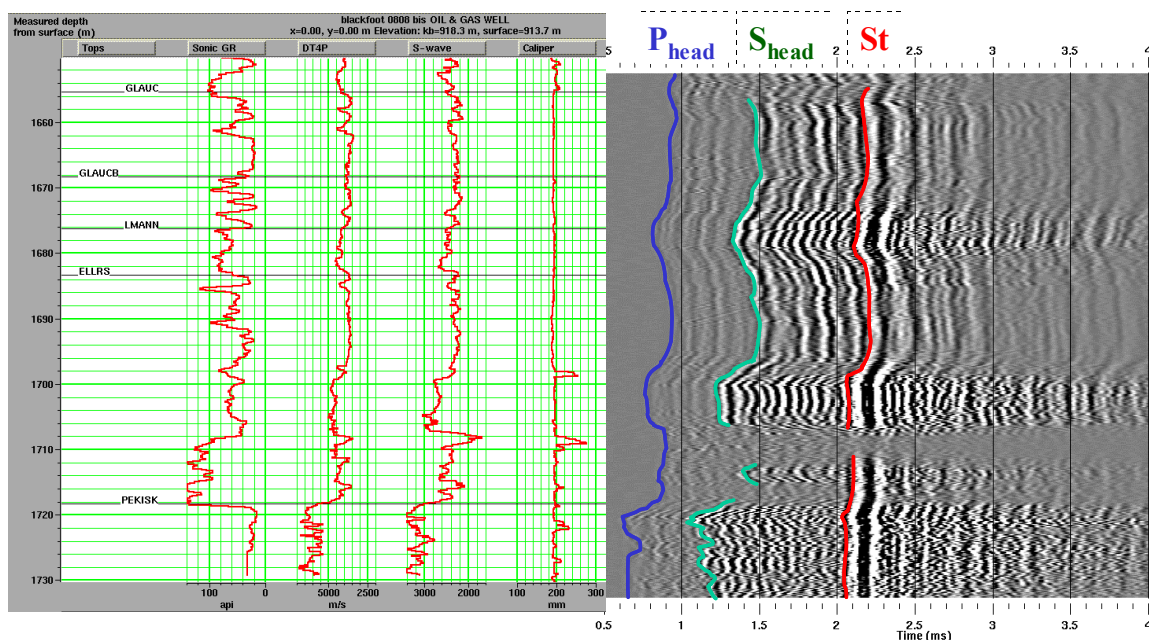
FIGURE 4.9. Open-hole well logs (left) and the corresponding full-waveform common-offset sonic section (at 3.05 m) from 0.5 to 4 ms over the depth interval of 1655 m to 1730 m. Formation tops present over the interval are Glauconitic sandstone (GLAUC), Ellerslie sandstone (ELLRS) and Pekisko limestone (PEKISK).

In the common-offset sonic sections shown in Figures 4.6 to 4.9, the observed interference patterns are probably all associated with bed boundaries. On the other hand, none of the interference patterns observed could be associated with Stoneley reflections.

Figure 4.10 shows two common-offset sections, over the same depth interval, where the top has a common offset of 2.74 m, while the bottom has a common offset of 3.81 m. Interfaces are first picked in the top display (horizontal reference lines) and next copied in the lower display unchanged (same horizontal reference lines). When comparing the top with the bottom display, at the corresponding horizontal reference lines, it can be observed that, for the greater offset, there is increased complexity or decreased continuity in the shape and character of the P-, S- and Stoneley-wave events.

First, the change in the relative onset-time pattern with offset can be explained by the different velocities of the P, S and Stoneley waves. Second, the change in the shape of these events at greater offset can be attributed to the greater distances travelled along the borehole wall and the greater variation in the rock properties encountered when the waves travel through more than one rock formation. In other words when a source-receiver pair lies in the same rock type at different position along the borehole axis, the onset event is smooth. However when that same pair spans different rock types, that same onset event becomes variable indicating that the P- and S-head waves traverse more and more diverse rock types. This behaviour of variations in the compressional and shear pseudo-Rayleigh events along the borehole axis could help better identify bed boundaries, where the highest confidence in the picked interface associated with bed boundaries would be on the common-offset gather with the shortest offset. Finally, as seen in Figure 4.10, the character of any single wave onset (numbers of peaks and troughs) also changes with increased offset. This could be indicative of the dispersive nature for a given wave-mode (e.g. Stoneley).

Although the common-offset section of the raw waveform data provides a powerful interpretation tool, it does not image the reflected energy that may be present in the records. Thus, in order to image reflections, I need to process the data further.

As a result, a 40-m section of the full-waveform dataset (Figure 4.8), which corresponds to 267 shot records, was selected. This section covers a segment of the borehole from a measured depth of 1590 m to 1630 m. In this segment, the borehole intersects three coal-seam interfaces at an angle of approximately 65° with respect to the borehole axis. These coal stringers have an average density of 1800 kg/m^3, an average

compressional velocity of 3000 m/s and an average shear velocity of 1800 m/s. They are surrounded by shaly formations with an average density of 2600 kg/m^3, an average compressional velocity of 4100 m/s and an average shear velocity of 2300 m/s. The processing of this portion of the full waveform is described in the next chapter.
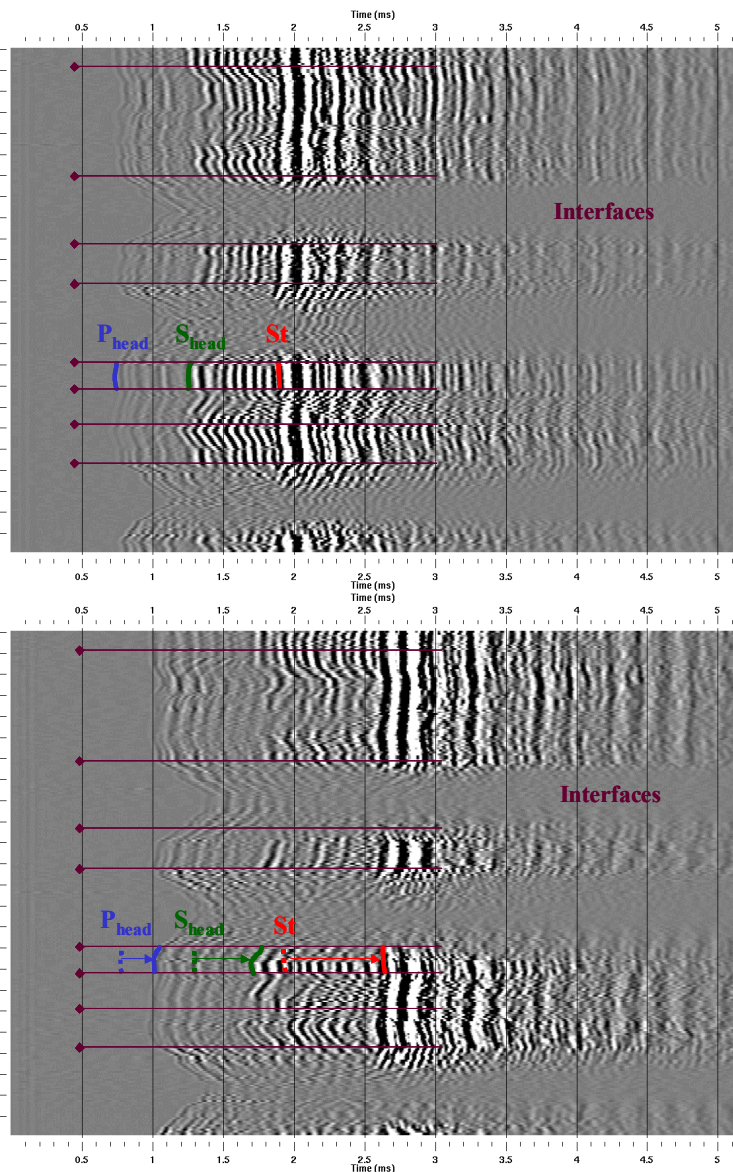
FIGURE 4.10. Comparison between a common-offset sonic section at 2.74 m (top) to one at 3.81 m (bottom) over the same time (0.5 to 5.12 ms) and depth interval (1590 to 1630 m).

CHAPTER 5: PROCESSING AND IMAGING OF SINGLE-WELL SONIC FULL WAVEFORM FIELD DATA

5.1 Processing of the full-waveform data

The waveform processing and imaging of the 40-m section (from 1590 m to 1630 m) of field data were done in this chapter. The problem with full-waveform data acquired with a conventional well-logging tool, in contrast to full-waveform data acquired with a research tool, is that in the former there is spatial aliasing and there are a limited number of offsets and traces per shot record. To address these problems, radial filtering (Henley, 1999) and the equivalent-offset method of prestack migration (Bancroft *et al.*, 1998) were selected in my processing flow. In addition, no detailed processing guidelines or 'rules of thumb' existed in the published literature for processing such a dataset and thus many parameters had to be created from scratch. The processing of the full-waveform data in a composite sonic image was done with Landmark's ProMAX™ software.

5.1.1 Geometry

Because there was no well-deviation data recorded, the borehole was assumed to be of a 2D straight-line geometry. The well-logging tool was assumed to have run centralized in the borehole. Thus, all the source and receivers elevations were set to zero so as to place them at the borehole axis, which is the datum. The borehole axis became the horizontal *x*-axis. This geometry assignment generated a regular fold pattern (maximum fold of 4) with a common-midpoint spacing of 0.075 m. Figure 5.1 present a

sample of five consecutive raw shot gathers taken from source depths of 1628.93 m to 1629.54 m.
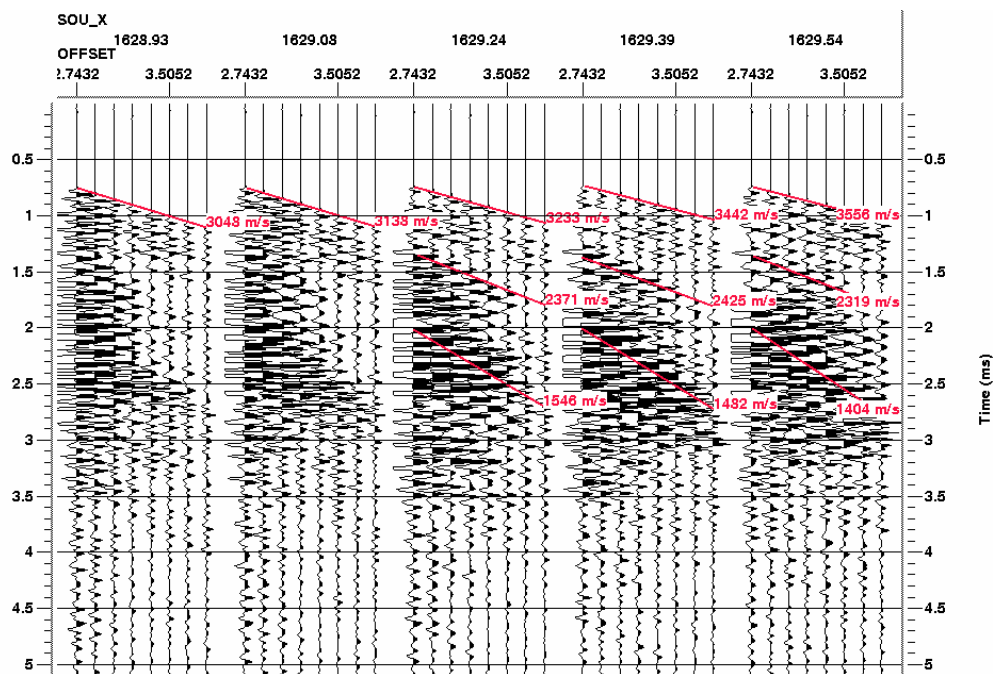
FIGURE 5.1. Raw sonic shot records showing the linear moveouts for the compressional (top event at ≈3280 m/s), the shear-pseudo-Rayleigh (middle at ≈2370 m/s) and the Stoneley arrivals (bottom at ≈1470 m/s). All traces have same scaling applied.

5.1.2   First-break picking and statics

Efforts were made, in this section, to identify in the reflections the presence of traveltime distortions caused by 'near-surface' irregularities and to attempt to remove those effects, if they were present and significant. In this processing step, I looked into the application of both 'field' and refraction statics to the full-waveform data.

In the case of field statics, I looked into subtracting a time delay, from each individual full-waveform trace, that was proportional to the sum of the distances measured between the reference of 100 mm (bit size radius) and the borehole wall at the

source and at the receiver location that was associated with the complete travel path for that particular waveform. Using a fluid velocity of 1500 m/s and the borehole caliper data, at maximum hole enlargement, the time shift on the full-waveform trace was less than 0.05 ms (5 time samples). These statics could, however, be significant and require correction using this method for boreholes with very uneven cross-sections.

In the case of refraction statics, I explored the effects of the variability of the near borehole. To achieve this, the first step consisted in picking first breaks on all the waveforms. Next, with the help Hampson-Russell's GLI3D™ and both 2- and 3-layers models, I explored the variability of the near borehole. This approach was inconclusive. Despite all these efforts, no static corrections were applied to the full-waveform dataset.

5.1.3 Trace balancing and mute

Trace balancing was applied in order to achieve about the same amplitudes at all times of the full-waveform traces. Because of the different attenuation mechanisms of the different borehole-wave modes, an automatic gain compensation (AGC) was used. An AGC operator length of 1 ms with an RMS scaling was applied. Note that I am interested in recovering the reflected events, not their true amplitudes. In addition, a trace mute from 0 to 0.4 ms was applied to all waveforms in order to remove road noise from the traces. Road noise is noise originating from the well-logging tool vibrations caused by its rubbing against the borehole wall and not from the acoustic propagation.

5.1.4 Filtering

The suppression and removal of the shear pseudo-Rayleigh, fluid and Stoneley waves from individual shot records were carried out with a series of radial dip filters

(Henley, 1999). Such filters have the advantage of focusing on localized events in the *x-t* domain, rather than on widespread families of events (as, e.g., *f-k* filters do). First a radial dip filter with a nominal filter velocity of 2200 m/s (with a ±200 m/s velocity range) was used to remove the shear pseudo-Rayleigh arrivals from the shot records. This step was followed by the application of a radial dip filter with a nominal filter velocity of 1450 m/s (with a ±150 m/s velocity range) to remove the Stoneley and direct fluid arrivals from the shot records. Because reflected Stoneley arrivals were suspected to be present in some shot records, a similar radial dip filter, with negative velocities, was applied. The dip filters were all applied in the common-shot domain only. Figure 5.2 shows the same sample shot records as shown in Figure 5.1 after the application of dip filters in cascade. Note the removal of the shear pseudo-Rayleigh and Stoneley.
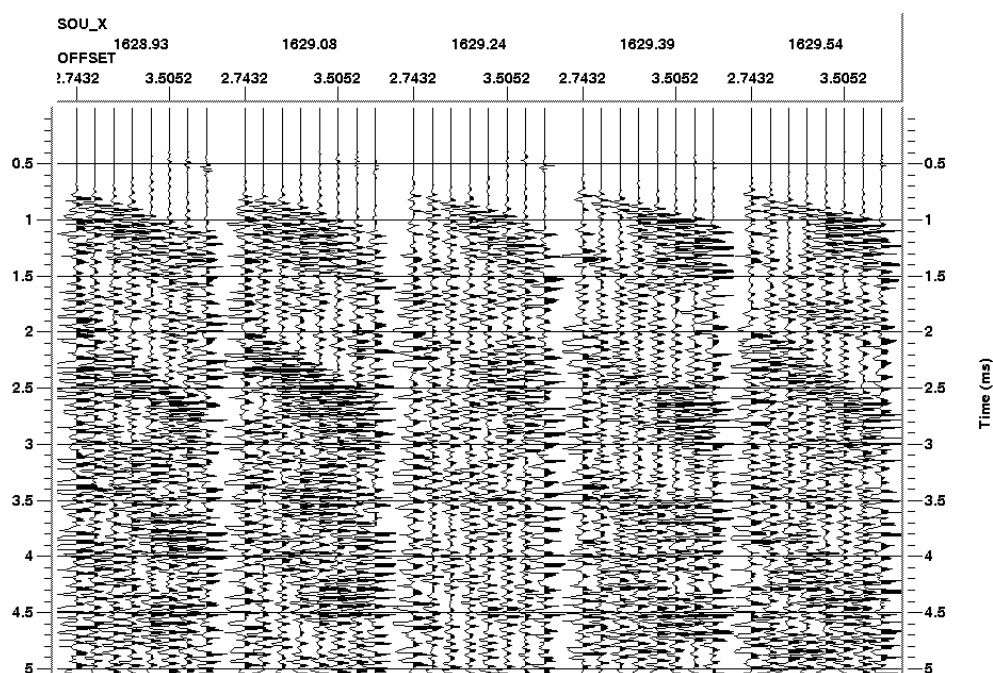
FIGURE 5.2. Five sonic shot gathers after the application of radial dip filter in cascade.

5.1.5 Deconvolution

Deconvolution attempts to collapse the illuminating waveform and maximize the resolution of the seismic image. It was noted in the common-offset sonic sections, shown in section 4.5, that there were multiple arrivals for the compressional, shear and pseudo-Rayleigh waves. The ringing observed after the onsets of the different wave modes could have been caused by several factors such as: the well-logging tool being excentered from the borehole axis; the borehole having a non-circular cross-section; multiple P-head waves reverberating in the borehole, and/or a ringy source. An autocorrelation analysis was next performed on those waveforms in order to identify parameters for the application of predictive deconvolution to attack the multiples in the full waveforms. After analysis, predictive deconvolution with an operator length of 0.25 ms, a prediction distance of 0.07 ms, and a white-noise level of 0.01 was selected. The deconvolved waveforms were filtered with an Ormsby bandpass filter with the following characteristics 5500-7333-20000-26667 Hz. Figure 5.3 shows the same sample shot records (Figure 5.1) after the application of filtering and deconvolution.
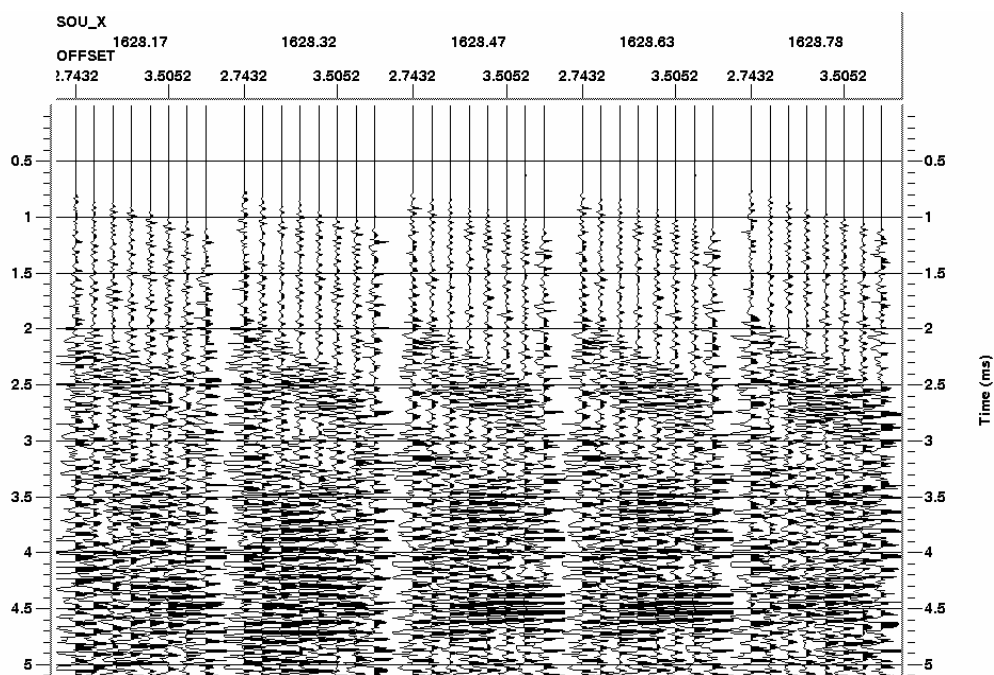
FIGURE 5.3. Five sonic shot gathers after the application of filtering and deconvolution.

5.1.6 Prestack time migration

The equivalent-offset method (EOM) of prestack time migration (Bancroft *et al.*, 1998) was next applied to the field data.

The first step consisted in forming two-sided common-scatter-point (CSP) gathers. Two-sided CSP gathers were formed for a positive and a negative equivalent offset distance of 7.6 to 10 m. A velocity of 3000 m/s was selected for the migration aperture. The equivalent-offset bin size was selected at 0.075 m. These values were selected because no steep dips were expected in the subsurface.

The two-sided CSP gathers were next split and arranged into two separate families of one-sided gathers (one set of CSP gathers consist of gathers with only positive equivalent offsets, while the other has only negative equivalent offsets). The CSP gathers with negative equivalent offsets, were arranged together representing the updip portion of

the interface crossing the borehole, while those with positive equivalent offsets, were arranged together representing the downdip portion of the interface crossing the borehole. Once this separation was completed, it was possible to conduct velocity analysis on the individual family of CSP gathers.

The first method is velocity semblance analysis. Attempts were made to pick a velocity function at a fixed distance interval along the borehole axis. Figure 5.4 shows a typical velocity analysis window where on the left the semblance plot is overlain by a white line that represents the velocity function, with picks, which has been applied to flatten the CSP gather on the right.
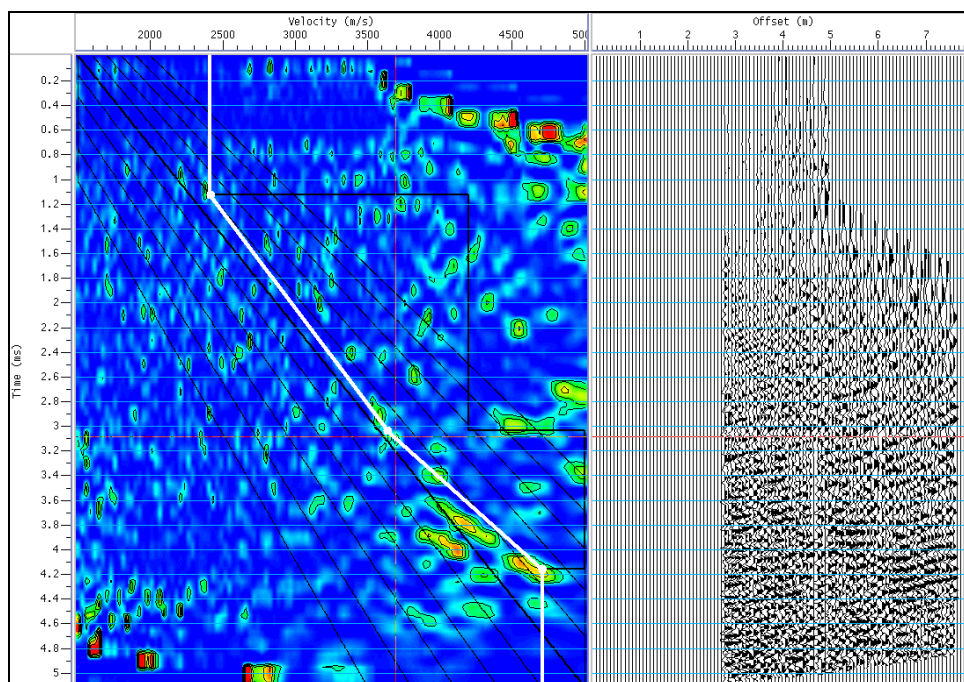
FIGURE 5.4. Velocity semblance analyses of the negative CSP gather number 2529.

The minimum and maximum semblance analysis values used were 1500 m/s and 5000 m/s respectively (the range of compressional stacking velocities). Note the advantage of the CSP gather, which has a larger offset range than the common-midpoint

(CMP) gather. Despite this advantage, I obtained a velocity function characterized by few picks (2 or 3 per panels) where each pick had a low confidence level in the semblance. Thus it was necessary to supplement this velocity function with the use of another method of velocity analysis.

The second method is constant-velocity stacks. A series of constant-velocity stacks were created from 1500 m/s to 5000 m/s (the range of compressional stacking velocities) in steps of 23 m/s. Figure 5.5 shows typical velocity stacks for the negative CSP gathers where it shows how the stack changes with the application of different NMO velocities (in this case 3014 m/s and 4033 m/s). After this analysis the final compressional stacking-velocity function to be applied to the CSP gathers for NMO correction, was created by combining the results of both methods of velocity analysis and the well-logging V_P dataset.
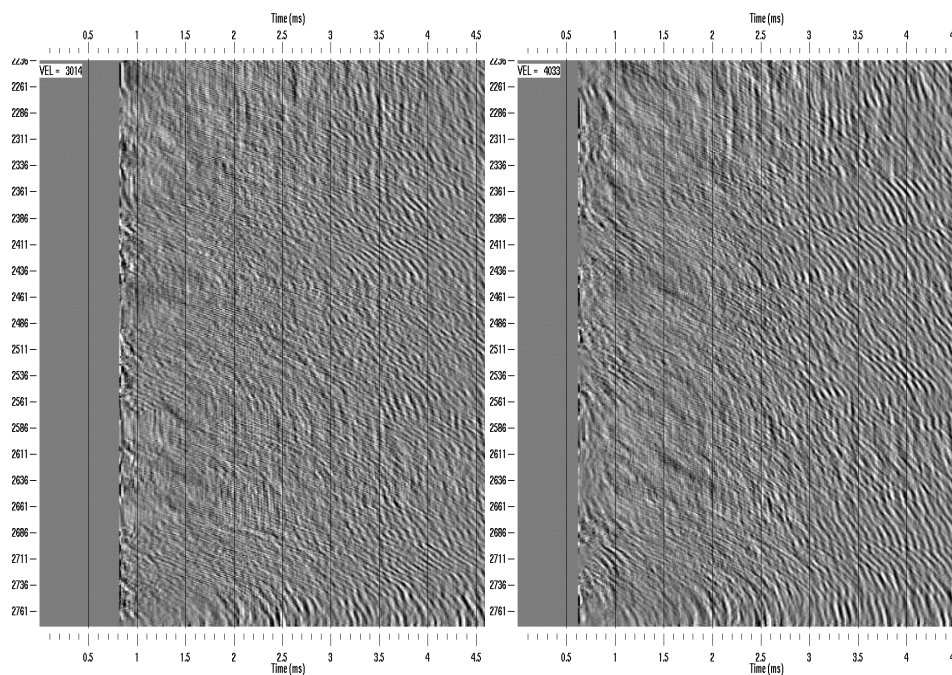
FIGURE 5.5. Constant velocity stacks for the negative CSP gathers for 3014 m/s on the left and 4033 m/s on the right.

I next applied NMO (50% stretch mute) using a velocity function to the CSP gathers with the negative equivalent offsets, followed by a conventional stack, thus forming the prestack time-migrated image of the updip region of the hole.

This was followed next by applying NMO (50% stretch mute), with the same velocity function, to the family of CSP gathers with the positive equivalent offsets, followed by a conventional stack, thus forming the prestack time-migrated image of the downdip region of the hole.

The two processed stacked sections were next combined along their common zero time, the datum, which in the final image becomes the borehole axis. The complete processing-imaging flow is shown in Figure 5.6. The final processing results are presented and discussed in the following section.

```
┌──────────────┐                    ┌──────────────────┐
│   Geometry   │───────────────────▶│ First break picking │
└──────────────┘                    └──────────────────┘
                                              │
                                              ▼
                                    ┌──────────────────┐
                                    │ (Static corrections) │
                                    └──────────────────┘
                                              │
                                              ▼
                                    ┌──────────────────────┐
                                    │ Trace balancing and mute │
                                    └──────────────────────┘
                                              │
                                              ▼
                                    ┌──────────────────┐
                                    │ Radial Dip Filtering │
                                    └──────────────────┘
                                              │
┌────────────────────────┐                   ▼
│ Autocorrelation analysis │◀──────▶│ Predictive Deconvolution │
└────────────────────────┘          └──────────────────────┘
                                              │
┌──────────────────┐                          ▼
│ Velocity analysis │◀──────────────▶│    CSP gathers    │
└──────────────────┘                 └──────────────────┘
                                              │
            Positive hₑ                       ▼          Negative hₑ
                                    ┌──────────────────┐
                                    │ Sorting CSP gathers │
                                    └──────────────────┘
                                     ┌──────┐    ┌──────┐
                                     │ NMO  │    │ NMO  │
                                     └──────┘    └──────┘
                                     ┌──────┐    ┌──────┐
                                     │Straight│   │Straight│
                                     │ stack │   │ stack │
                                     └──────┘    └──────┘
            Downdip                  ┌────────────────────┐   Updip
                                     │ Composite sonic image │
                                     └────────────────────┘
```

Positive h_e Negative h_e
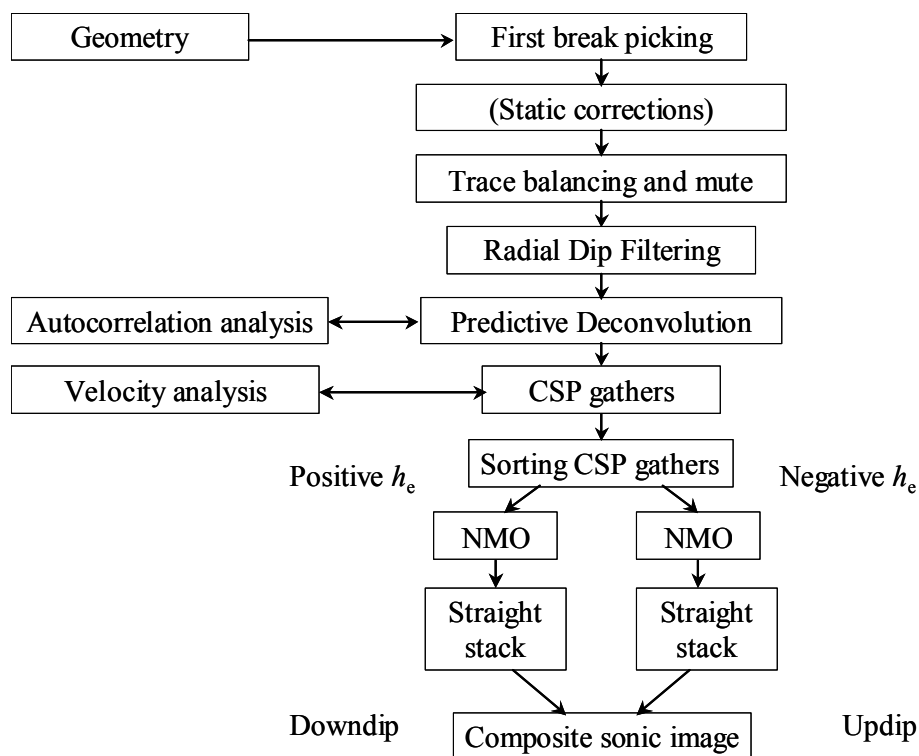
FIGURE 5.6. Flowchart of the processing flow used to transform full waveforms into an image of the acoustic impedance contrasts away from the borehole wall.

5.2   Composite sonic image

This section presents the results of the processing of the 40-m section of full-waveform data from the 08-08 well. Several composite sonic images are presented in this section (Figures 5.7 to 5.10). Each figure displays the same data but with slightly different processing parameters applied to it. Each figure attempts in its own way to image the three coal seams intersecting the borehole. Each figure is composed of two parts: the prestack time-migration image of the full-waveform data or the composite sonic image (on the left) and the computed impedance and reflectivity from the open-hole well logs (on the right). The vertical interval shown here is 40 m. The lateral extent of investigation away from either side of the borehole wall, is 5.12 ms. In these images, the colours blue, white and red represent negative, zero and positive amplitudes, respectively. The vertical-to-horizontal scale of the composite sonic image is 1:1 (approximately).

The horizontal resolution (parallel to the borehole axis) of the composite sonic sections can be calculated using the Sheriff (1980) criterion. The diameter of the first Fresnel zone for P-waves, R_{FP}, is given by:

$$R_{FP} \approx V_P \left(t_{0P}\, T \right)^{1/2} \tag{5.1}$$

where T is the dominant period and t_{0P} is the two-way traveltime. Using a t_{0P} of 5.12 ms, a frequency of 20 kHz and a compressional velocity of 4000 m/s, one obtains a Fresnel-zone diameter of 2.02 m, that is, about 2 m. Migration improves the resolution diameter inline to 0.05 m (best case).

Figure 5.7 presents the initial processing results using an equivalent offset of 10 m in the EOM method. Note that there is no bandpass filter or AGC applied to the data. The

arrows point out possible reflections. The weak amplitude bands in the section can identify the presence of the three coal seams in the composite sonic image.
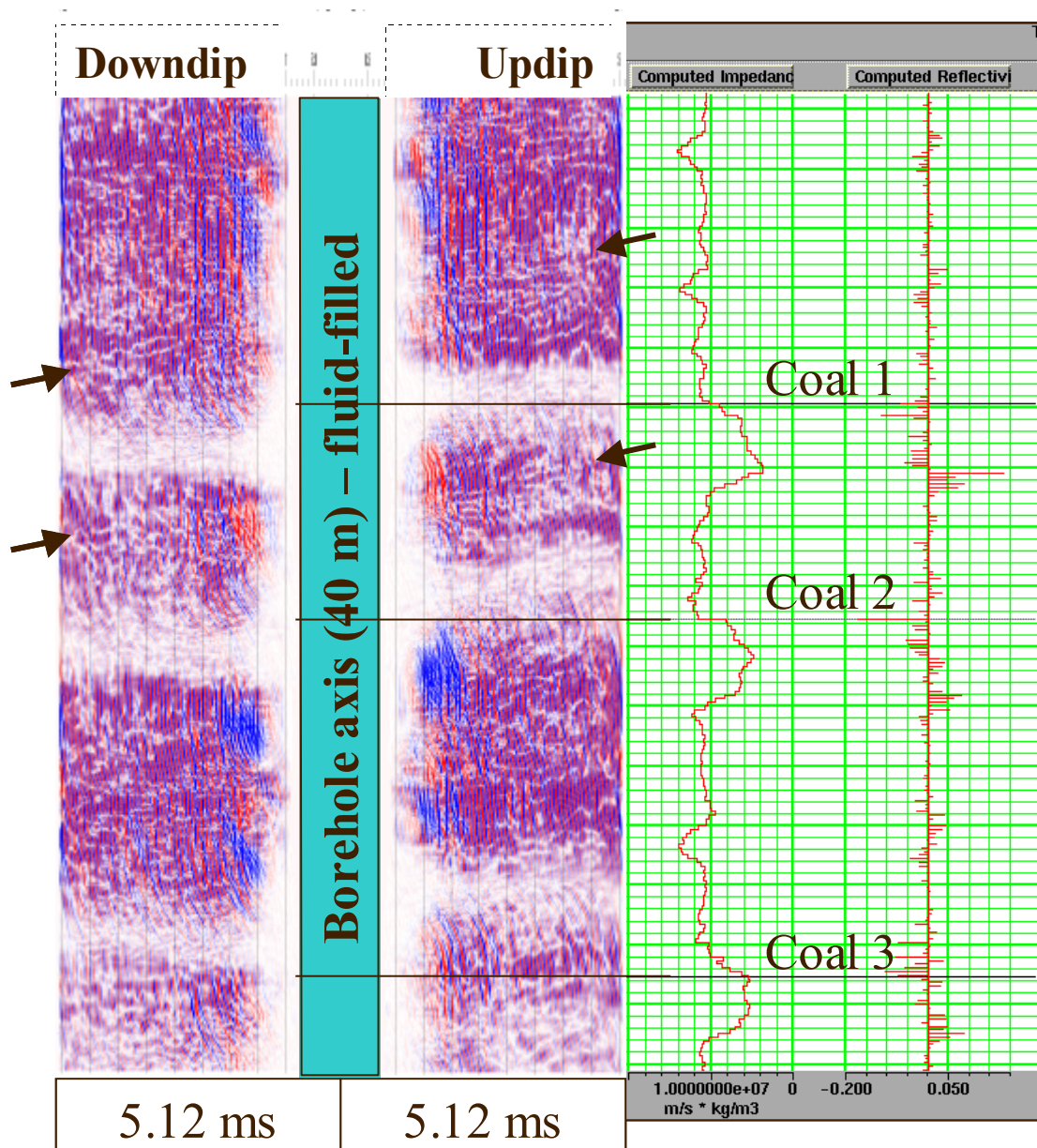
FIGURE 5.7. Composite sonic image with an equivalent offset of 10 m. There is no final bandpass filter or AGC applied to this image.

Figure 5.8 presents the processing results using a shorter equivalent offset of 7.6 m. A constant velocity function of 3500 m/s was used for the NMO correction of the CSP gathers. The final image was bandpassed to 3-8-22-27 kHz with an AGC of 2 ms. The arrows point out potential reflections.
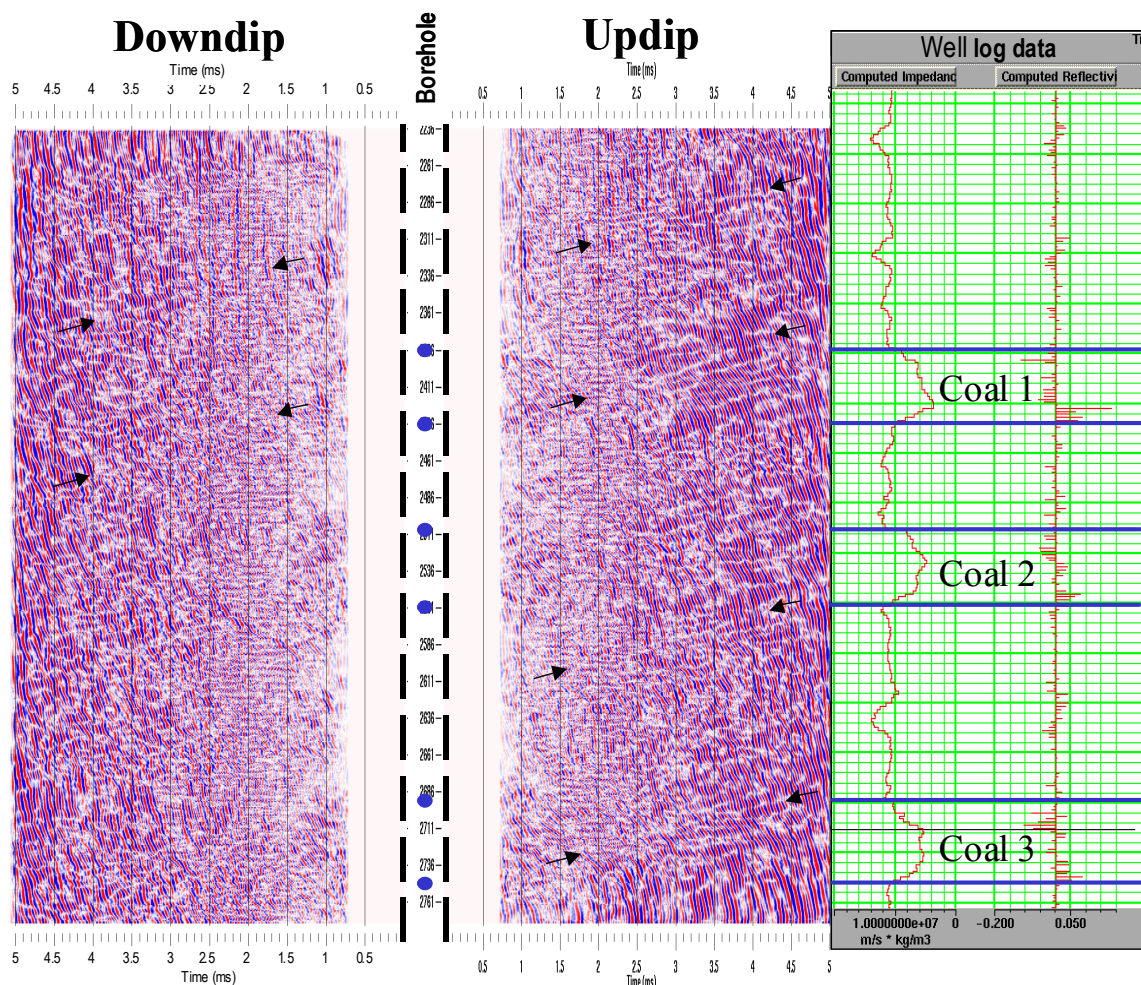
FIGURE 5.8. Composite sonic image with an equivalent offset of 7.6 m. A constant velocity function of 3500 m/s was used for the NMO correction. The final image was bandpassed to 3-8-22-27 kHz with an AGC of 2 ms.

Figure 5.9 present the processing results with the same equivalent offset of 7.6 m but using instead a constant velocity of 4000 m/s for NMO correction. The final image was bandpassed to 3-8-22-27 kHz with an AGC of 2 ms. The arrows point out possible reflections. This is potentially the best image.
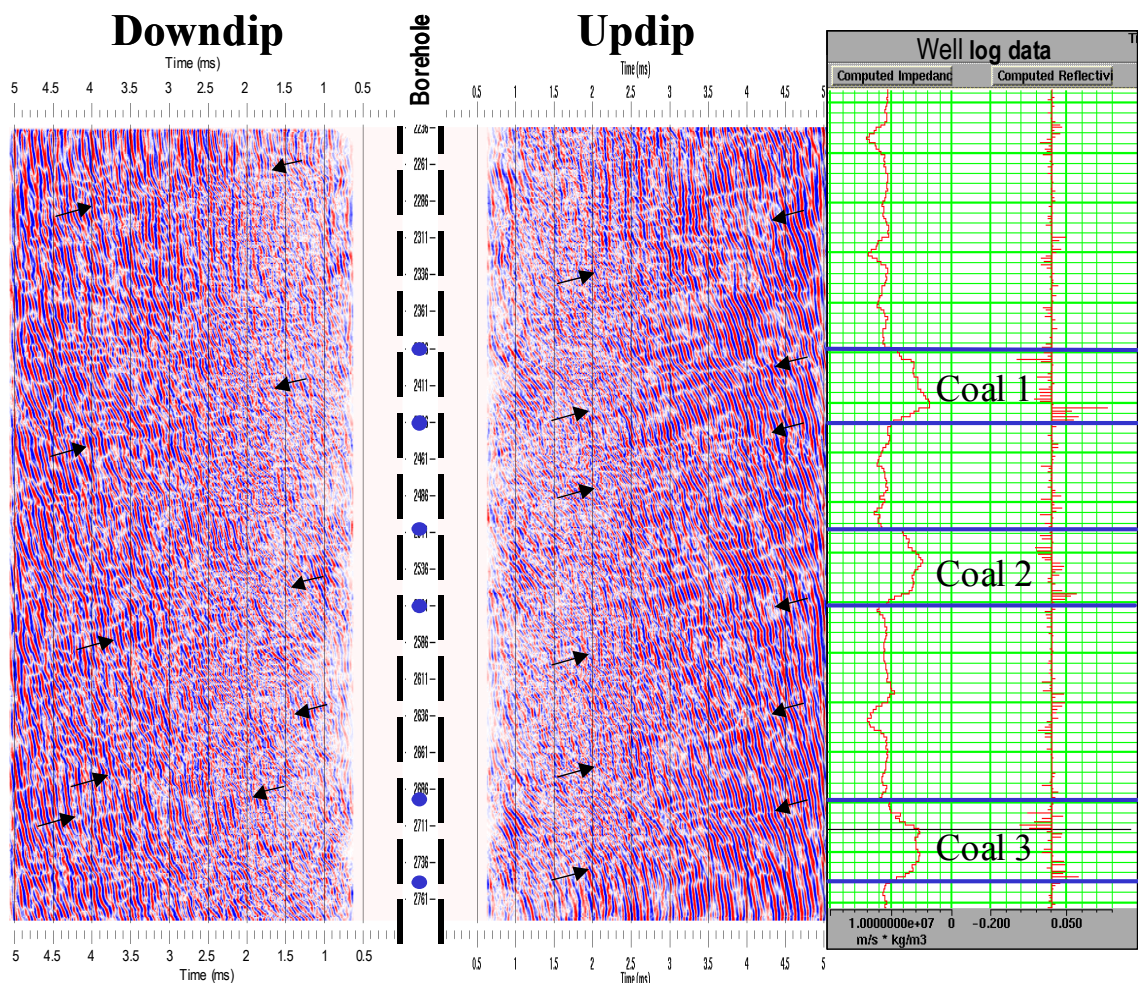
FIGURE 5.9. Composite sonic image with an equivalent offset of 7.6 m. A constant velocity function of 4000 m/s was used for the NMO correction. The final image was bandpassed to 3-8-22-27 kHz with an AGC of 2 ms.

Finally, Figure 5.10 show the results using an equivalent offset of 7.6 m and NMO-corrected gathers using the variable velocity function derived from the velocity analysis step. The final image was bandpassed to 3-8-22-27 kHz with an AGC of 2 ms. Again the arrows point out potential reflections.
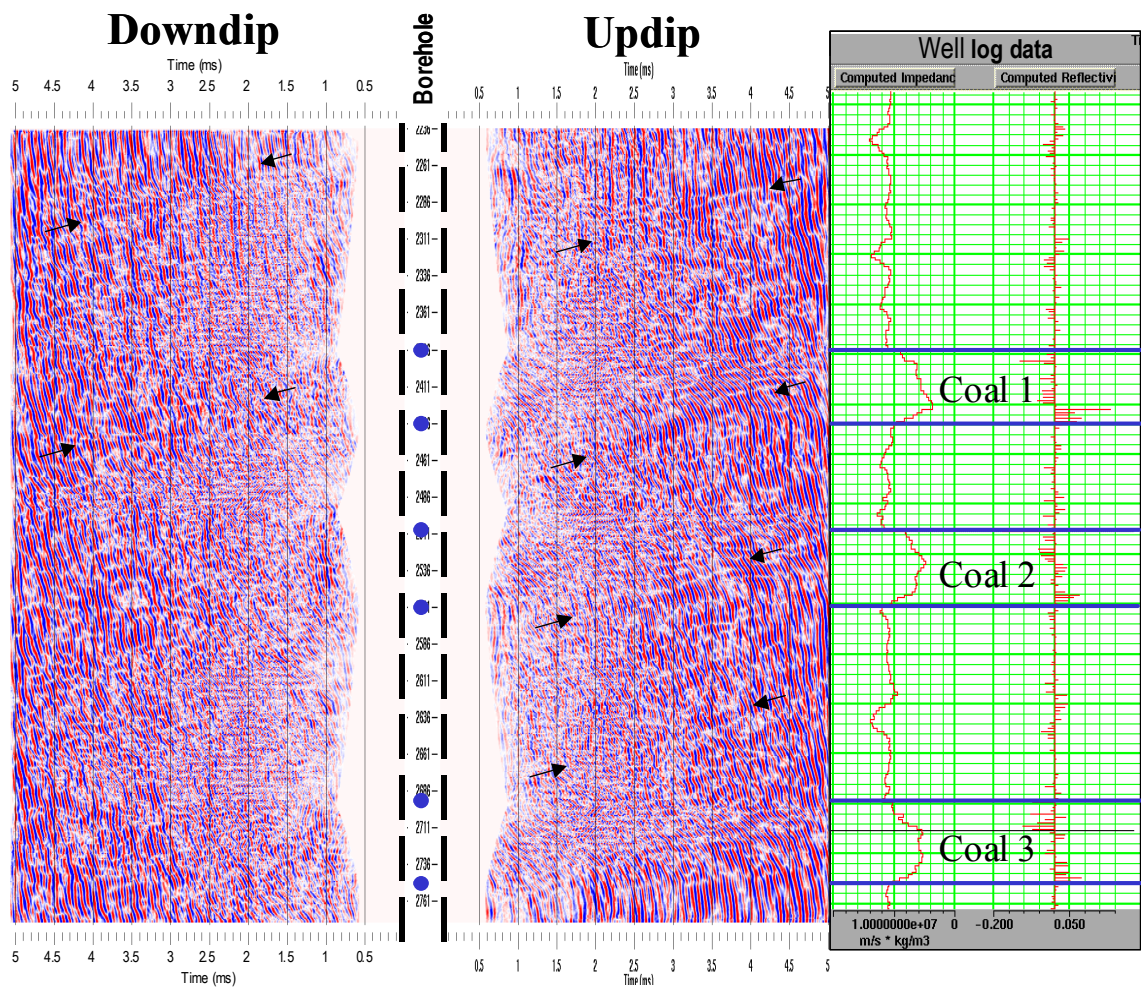
FIGURE 5.10. Composite sonic image with an equivalent offset of 7.6 m. The velocity function derived in the velocity analysis step was used for the NMO correction. The final image was bandpassed to 3-8-22-27 kHz with an AGC of 2 ms.

CHAPTER 6: COMPARISON WITH SURFACE SEISMIC DATA

In order to verify the accuracy of the composite sonic image obtained by the imaging-processing flow of the previous chapter, it was next necessary to compare those results with another image of the same borehole but acquired by a different method. Since no Formation MicroScanner Imaging (FMS), no Fullbore Formation MicroImager (FMI) logs, and no dipmeter data were acquired for this well, which would have provided the dips and azimuths of beds relative to the borehole axis, it was important that I find an alternate method of validating independently my results. The next best thing, although less than optimal, was to compare the composite sonic image with the surface seismic data at the well location.

A vertical-component seismic section was extracted from the 3C-3D surface-seismic volume that was acquired over the Blackfoot field in 1995 at the 08-08 well location, intersecting the deviated borehole trajectory. The extracted seismic data have the following characteristics: a 30-m bin size, a CDP fold of 10 to 17, and a final bandwidth of 10 to 80 Hz.

Figure 6.1 shows the extracted seismic section at the 08-08 well location. The surface location of the 08-08 well is represented by a solid dot. The synthetic seismogram, using the 08-08 well-log information, is located in its true vertical position at depth, underneath the solid dot. The approximate deviated well trajectory is highlighted on the seismic section by a dipping straight solid line. The 40-m borehole segment, corresponding to the composite sonic image of Figure 5.9, is shown on the well trajectory.

The seismic section in Figure 6.1 shows that the regional geology near the well is generally flat. In addition, the three coal seams associated with zero-amplitude crossings in the seismic section (Figure 6.1) hardly have the same amplitude characteristics in the composite sonic image (Figure 5.9).
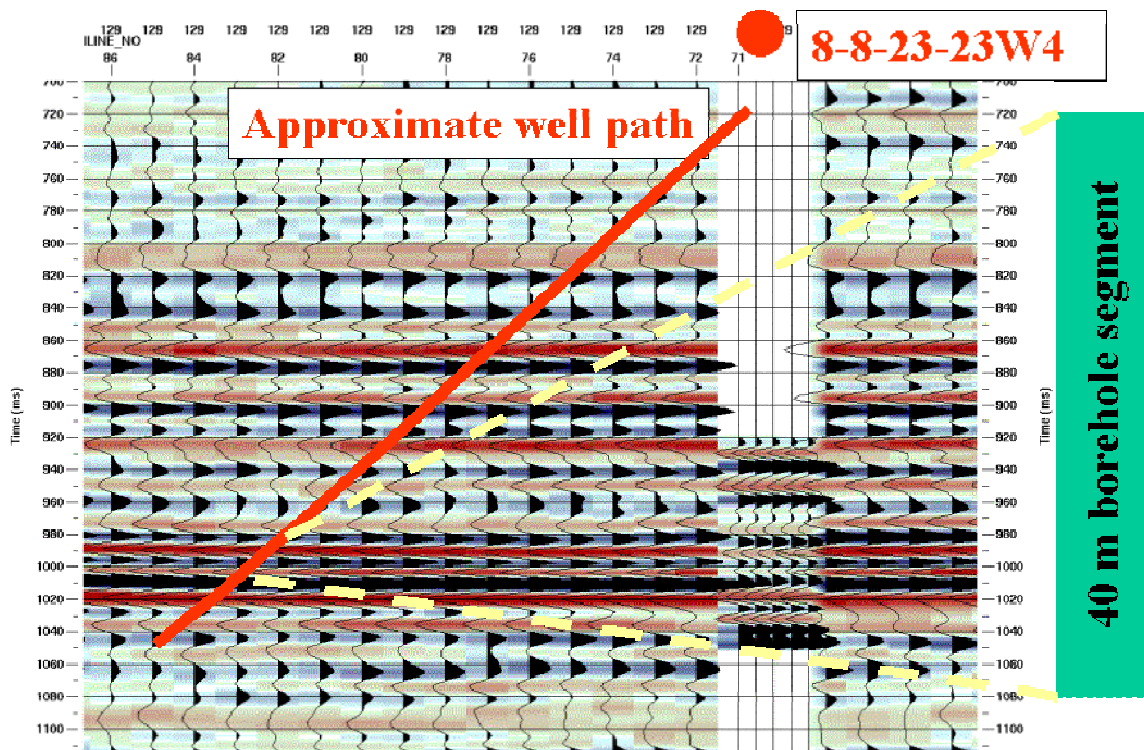
FIGURE 6.1. Seismic section (vertical component) intersecting the deviated borehole along its dip direction. The time axis of the seismic section extends from 700 ms to 1120 ms.

In comparing, at the well location, the composite sonic image (Figure 5.9) with the seismic section (Figure 6.1), the problem of scale and resolution becomes apparent. In fact, it is difficult at best to validate the results using this approach. This reinforces the problem associated with the resolution gap discussed in Chapter 1 and shown in Figure 1.2. No further validation of the composite sonic image could be made.

CHAPTER 7: CONCLUSIONS AND FUTURE WORK

An imaging-processing flow for full-waveform sonic data has been proposed and tested on the full-waveform sonic data of the 08-08 well of the Blackfoot field. This imaging-processing flow incorporates improved filtering and imaging steps relative to those of previous work. These improvements include the use of radial filtering, for better attenuation of the borehole modes with linear moveouts, and the use of EOM for the prestack time migration of the reflected energy.

The final composite sonic images presented in the previous chapter look promising, with the identification of possible reflections at some distance from the borehole wall. These reflections, which are not seen in surface seismic, add to our knowledge of the reservoir. The final composite image obtained in this work, however, experienced difficulties showing the reflections from the expected three dipping coal seams intersecting the borehole at an angle. Many factors could account for this.

First, the fractured coal units may have attenuated or trapped the energy from the source of the well-logging tool as it crossed the coals, thereby making that energy unavailable for imaging. Note that the zone of amplitude reduction of the arrivals corresponds to a transmitter-receiver spacing of roughly 3 m. Second, many noise modes may have been incompletely cancelled in the processing, thus reducing the relative strength of the signal over the noise. Finally, the combination of weak reflecting boundaries and the large angle (~65°) between the borehole axis and the surface of the geological interfaces probably caused additional weakness in the reflections.

It is important to be reminded that results from single-well sonic imaging need to be interpreted in conjunction with other borehole data. It is not a stand-alone method. For example, additional well data, such as dipmeter information, would have been helpful in rotating the final sonic image to its proper azimuthal orientation relative to the borehole and the reservoir. This method will probably not be able to resolve an image in geologically complex reservoirs but is applicable in imaging simple geological/geometrical shapes present in the reservoir.

The sonic-waveform processing-and-imaging flow presented in this thesis could benefit from additional numerical-modelling experiments where the responses of reflectors of various acoustic-impedance contrasts, dip angles and shapes to the sonic wave propagation in the borehole could be studied.

The processing-and-imaging flow presented in this thesis could be improved further by the addition of a proper migration datum to capture the deviated nature of the borehole, when detailed deviation data are available. Also, an improved weighting function could be used in EOM in order to better preserve the amplitudes (Geiger 2002).

The proposed processing flow could be tested on a more favourable sonic full-waveform dataset. The optimal dataset should consist of full waveforms acquired in a well where the borehole axis intersects the surface of the beds at an angle of 35° or less. This dataset should also include a full suite of well logs including resistivity borehole-imaging data (e.g. FMI) and vertical-seismic-profiling data to validate the composite sonic image independently. The improved sonic imaging-processing flow could be further applied to full-waveform field data acquired with a dipole source or in cased-hole.

REFERENCES

Arditty, P.C., Arens, G., and Staron, P., 1981, EVA: A long spacing sonic tool for evaluation of velocities and attenuations: 51st Ann. Internat. Mtg. Soc. Expl. Geophys., Expanded Abstracts.

Bancroft, J.C., Geiger, H.D., and Margrave, G.F., 1998, The equivalent offset method of prestack time migration: Geophysics, **63**, 2042 - 2053.

Bancroft, J.C., and Xu, Y., 1999, Equivalent offset migration for vertical receiver arrays: 69th Ann. Internat. Mtg. Soc. Expl. Geophys. Expanded Abstracts, 1374-1377.

Basick, J.T., 1983, Ray tracing and full acoustic waveform analysis, Research and development report, Phillips Petroleum company, 59 pages.

Biot, M.A., 1952, Propagation of elastic waves in a cylindrical bore containing a fluid: Journal of Applied Physics, **23**, 997-1005.

Brie, A., Endo, T., Johnson, D.L., and Pampuri, F., 2000, Quantitative formation permeability evaluation from Stoneley waves: SPE Reservoir Eval. & Eng., **3**, 109-117.

Brown, R.J., Stewart, R.R., and Lawton, D.C., 2002, A proposed polarity standard for multicomponent seismic data: Geophysics, **67**, 1028-1037.

Chang, C., Hoyle, D., Watanabe, S., Coates, R., Kane, M., Dodds, K., Esmersoy, C. and Foreman, J., 1998, Reservoir maps from the borehole: Oilfield Review, **10**, 56-66.

Chen, S.T., 1993, A single-well profiling tool and tube-wave suppression: 63rd Ann. Internat. Mtg. Soc. Expl. Geophys. Expanded Abstracts.

Cheng, C.H. and Toksöz, M.N., 1981, Elastic wave propagation in a fluid-filled borehole and synthetic acoustic logs: Geophysics, **46**, 1042-1053.

Cheng, N., Cheng, C.H. and Toksöz, M.N., 1995, Borehole wave propagation in three-dimensions: Journal of the Acoustical Society of America, **97**, 3483-3493.

Claerbout, J.F., 1984, Imagingthe Earth's interior: Blackwell Scientific Publications.

Coates, R., Kane, M., Chang, C., Esmersoy, C., Fukuhara, M. and Yamamoto, H., 2000, Single-well sonic imaging: High-definition reservoir cross-sections from horizontal wells: SPE paper **65457**.

Dennis, B., 1985, Digital sonic (SDT): Full waveform logging applications in western Canada: Canadian Well logging Society Journal, **14**, 63-74.

Dennis, B., Standen, E., Georgi, D.T., and Callow, G.O., 1987, Fracture identification and productivity predictions in a carbonate reef complex: SPE paper **16808**.

Ebrom, D.A., and McDonald, J.A., 1994, Seismic physical modeling: Society of Exploration Geophysicists, Geophysics Reprint series No. 15, 519 pages.

Esmeroy, C., Chang, C., Kane, M.R., Coates, R.T., Tichelaar, B. and Quint, E., 1998, Acoustic imaging of reservoir structure from a horizontal well: The Leading Edge, **17**, 940-946.

Fortin, J.P., Rehbinder, N. and Staron, P., 1991, Reflection imaging around a well with the EVA full waveform tool: The Log Analyst, **32**, 271-278.

Geiger, H.D., 2002, Amplitude-preserving weights for Kirchhoff prestack time migration: 72nd Ann. Internat. Mtg. Soc. Expl. Geophys., Expanded abstracts.

Guevara, Saul E., 2001, Analysis and filtering of near-surface effects in land multicomponent seismic data: M.Sc. thesis, University of Calgary.

Harrison, A.R., Randall, C.J., Aron, J.B., Morris, C.F., Wignall, A.H., Dworak, R.A., Rutledge, L.L. and Perkins, J.L., 1990, Acquisition and analysis of sonic waveforms from a borehole monopole and dipole source for the determination of compressional and shear speeds and their relation to rock mechanical properties and surface seismic data: SPE paper **20557**.

Haugen, G.U. and Schoenberg, M.A., 2000, The echo of a fault or fracture: Geophysics, **65**, 176-189.

Henley, D.C., 1999, The radial trace transform: an effective domain for coherent noise attenuation and wavefield separation: 69th Ann. Internat. Mtg. Soc. Expl. Geophys. Expanded Abstracts, 1204-1207.

Hornby, B.E., 1989, Imaging of near-borehole structure using full-waveform sonic data: Geophysics, **54**, 747-757.

Hornby, B.E., Johnson, D.L., Winkler, K.W., and Plumb, R.A., 1987, Fracture evaluation from the borehole Stoneley wave: 57th Ann. Internat. Mtg. Soc. Expl. Geophys., Expanded Abstracts, 688-691.

Jorden, J.R., and Campbell, F.L., 1986, Well logging II – Electric and acoustic logging: Monograph **10**, Society of Petroleum Engineers, 182 pages.

Levander, A.R., 1988, Fourth-order finite-difference P-Sv seismograms: Geophysics, **53**, 1425-1436.

Lines, L.R., Slawinski, R. and Bording, R.P., 1999, A recipe for stability of finite-difference wave-equation computations: Geophysics, **64**, 967-969.

Liu, Q.-H., Schoen, E., Daube, F., Randall, C., Liu, H.-L. and Lee, P., 1996, A three-dimensional finite difference simulation of sonic logging: Journal of the Acoustical Society of America, **100**, 72-79.

Miller, D., Oristaglio, M., and Beylkin, G., 1987, A new slant on seismic imaging: Migration and integral geometry: Geophysics, **52**, 943-964.

Miller, S., Aydemir, E.Ö. and Margrave G.F., 1995, Preliminary interpretation of P-P and P-S seismic data from the Blackfoot broad-band survey: CREWES Research Report, 7, 42-1.

Morris, R.L., Grine, D.R. and Arkfeld, T.E., 1964, Using compressional and shear wave acoustic amplitudes for the location of fractures: Journal of Petroleum Technology, 623-632

Paillet, F.L. and Cheng, C.H., 1991, Acoustic waves in boreholes: CRC Press, 264 pages.

Paillet, F.L. and White, J.E., 1982, Acoustic modes of propagation in the borehole and their relationship to rock properties: Geophysics, **47**, 1215-1228.

Peveraro, R.C.A., Leavy, P.C. and Crampin, S., 1994, Single-well wideband borehole seismics in the UNIWELL configurations: an approach to monitoring hydrocarbon production: SPE paper **28854**.

Schlumberger, 1997, DSI™ – Dipole Shear Sonic Imager: Corporate brochure SMP-9200, 36 pages.

Sheriff, R.E., 1980, Nomogram for Fresnel-zone calculation: Geophysics, **45**, 968-972.

Sheriff, R.E. and Geldart L.P., 1995, Exploration Seismology: Cambridge University Press, 592 pages.

Tsang, L. and Rader, D., 1979, Numerical evaluation of transient acoustic waveforms due to a point source in a fluid-filled borehole: Geophysics, **44**, 1706-1720.

Tubman, K.H., Cheng, C.H., Cole, S.P., and Toksoz, M.N., 1986, Synthetic full waveform acoustic logs in cased hole, poorly bonded casing: Geophysics, **51**, 902-913.

Watanabe, S., Fujii, K. and Mikada, H., 1998: Reflector imaging using Borehole Acoustic Reflection Survey, Proceedings of the Fourth Well Logging Symposium of Japan, Soc. Prof. Well Log Anal., paper **Q**.

Willis, M.E., and Toksöz, M.N., 1983, Automatic P and S velocity determination from full waveform digital acoustic sonic logs: Geophysics, **48**, 1631-1644.

Yoon, K.-H. and McMechan, G.A., 1992, 3-D finite-difference modeling of elastic waves in borehole environments: Geophysics, **57**, 793-804.